

# Thesis Title

by

E. Ross



A thesis submitted to the  
University of Birmingham  
for the degree of  
DOCTOR OF PHILOSOPHY

Solar and Stellar Physics Group (SASP)  
School of Physics and Astronomy  
University of Birmingham  
Birmingham, B15 2TT  
Month 20XX

# Abstract

You're awesome. Make sure the examiners know it

# Acknowledgements

Who do you hate least?

# Contents

<b>Abstract</b>	i
<b>Acknowledgments</b>	ii
<b>List of Figures</b>	vi
<b>List of Tables</b>	vii
<b>List of Abbreviations</b>	viii
<b>1 HiSPARC as a Space Weather Detector</b>	1
1.1 Introduction . . . . .	1
1.1.1 Space Weather Effects . . . . .	2
1.1.2 HiSPARC Project . . . . .	2
1.1.3 HiSPARC Detector and Station Configuration . . . . .	2
1.2 Aims . . . . .	8
1.3 HiSPARC Properties . . . . .	9
1.4 HiSPARC Observations . . . . .	12
1.4.1 HiSPARC Observations of Ground Level Enhancements . . . . .	14
1.4.2 HiSPARC Observations of Forbush Decreases . . . . .	16
1.5 Air Shower Simulations . . . . .	19
1.5.1 Air Shower Footprints . . . . .	20
1.5.2 Muon Flux . . . . .	21
1.5.3 Muon Flux From MAIRE . . . . .	23
1.6 Standardisation of HiSPARC Data . . . . .	25
1.6.1 Motivation . . . . .	25
1.6.2 Barometric Correction . . . . .	25
1.6.3 Temperature Correction . . . . .	28
1.7 HiSPARC Observations After Pressure Corrections . . . . .	30
1.7.1 Pressure Corrected Observations of Ground Level Enhancements	30
1.7.2 Pressure Corrected Observations of Forbush Decreases . . . . .	31
1.8 Discussion . . . . .	32
1.9 Conclusion . . . . .	32

<b>2 HiSPARC Station 14008</b>	<b>34</b>
2.1 Introduction . . . . .	34
2.2 Aims . . . . .	35
2.3 HiSPARC 14008 Detector Set-up . . . . .	35
2.3.1 Configuration . . . . .	35
2.3.2 Calibration . . . . .	36
2.3.3 Monitoring Temperature . . . . .	37
2.4 Observations . . . . .	38
2.5 Conclusions . . . . .	39
<b>A Simulations of Cosmic Ray Air Showers using CORSIKA</b>	<b>40</b>
<b>Bibliography</b>	<b>44</b>

# List of Figures

1.1	Schematic diagram of the HiSPARC scintillation detector. (A): PMT; (B): light-guide adaptor; (C): light-guide; (D): scintillator. . . . .	3
1.2	Typical formations of two-detector and four-detector stations. In each, the grey circle denotes a GPS antenna which is located in between the detectors to provide a precise timestamp for each signal. . . . .	5
1.3	(a): An example PMT signal after digital conversion by the HiSPARC electronics box. The horizontal lines denote: the noise cut-off (dotted line), which is used for setting a limit when integrating the pulse height, to give the pulse integral; the low-voltage threshold (dash-dot); the high-voltage threshold (dashed). (b) The pulse height distribution over the course of a single day from HiSPARC station 501. The vertical lines show the low-voltage threshold (dash-dot) and the high-voltage threshold (dashed). . . . .	6
1.4	Azimuthal and zenith angle variations in the allowed and forbidden rigidity trajectories for HiSPARC station 501. . . . .	11
1.5	The vertical asymptotic viewing directions of 5 HiSPARC stations. The rigidity range of the simulations were from $1.0 \text{ GV} < R < 20.0 \text{ GV}$ , and the results are plotted in geographic coordinates on January 20th 2005. The diamonds correspond to the HS ground location and the circles correspond to the AVD for a specific rigidity value. . . . .	12
1.6	GLEs observed by the NM stations based at Oulu. Top panel: GLE 70; middle panel: GLE 71, bottom panel: GLE 72. The solid-black line shows the 2-minute-averaged, pressure corrected data and the vertical, dashed-red lines show the epochs of each GLE onset. . . . .	13
1.7	FDs observed by the NM stations based at Oulu. Top left panel: FDs during March 2012; top right panel: FD during July 2012, bottom left panel: FD during December 2014; bottom right panel: FD during September 2017. The solid-black line shows the 2-minute-averaged, pressure corrected data and the vertical, dashed-blue lines show the epochs of each FD onset. . . . .	14
1.8	HiSPARC data for stations 501 and 3001 around the epoch of GLE 70. The plot shows the minute-averaged and 5-minute-averaged trigger events between detectors within the station. The vertical red, dashed line depicts the approximate onset time of the GLE. The units of time on the x-axis are, MM-DD HH. . . . .	15

1.9	HiSPARC data for stations 8001 and 3001 around the epoch of GLE 71. The plot shows the minute-averaged and 5-minute-averaged trigger events between detectors within the station. The vertical red, dashed line depicts the approximate onset time of the GLE. The units of time on the x-axis are, MM-DD HH. . . . .	15
1.10	HiSPARC data for 4 stations around the epoch of GLE 72. The top panel of each subplot shows the minute-averaged trigger events between detectors within the station, while the bottom panel shows the mean-shifted, minute-averaged counts by each individual detector in the station. The vertical red, dashed line depicts the approximate onset time of the GLE. The units of time on the x-axis are, MM-DD HH. . . . .	16
1.11	HiSPARC data for stations 501 and 8001 around the epoch of the FDs in March 2012. The plot shows the minute-averaged and hourly-averaged trigger events between detectors within the station. The vertical blue-dashed lines show the approximate onset-time of the FDs. . . . .	17
1.12	HiSPARC data for stations 501 and 8001 around the epoch of the FD in July 2012. The plot shows the minute-averaged and hourly-averaged trigger events between detectors within the station. The vertical blue-dashed line shows the approximate onset-time of the FD. . . . .	17
1.13	HiSPARC data for 4 stations around the epoch of the FD in December 2014. The plot shows the minute-averaged and hourly-averaged trigger events between detectors within the station. The vertical blue-dashed line shows the approximate onset-time of the FD. . . . .	18
1.14	HiSPARC data for [n] stations around the epoch in which there were several FDs close to the onset of GLE 72. The top panel of each subplot shows the minute-averaged trigger events between detectors within the station, while the bottom panel shows the mean-shifted, minute-averaged counts by each individual detector in the station. The vertical blue-dashed lines show the approximate onset-times of the two FDs observed around this epoch and the red-dashed line depicts the approximate onset time of the GLE. . . . .	19
1.15	Mean muon density footprints for (a) proton-initiated air showers and (b) $\alpha$ -particle-initiated air showers with initial PCR trajectories with zenith angles $\theta = 0^\circ$ and various PCR energies. The error bars given represent $1\sigma$ . . . . .	21
1.16	Mean number of muons produced at ground level by the PCR for (a) proton-initiated air showers and (b) $\alpha$ -particle-initiated air showers, for various PCR energy. . . . .	22
1.17	Muon differential flux computed using CORSIKA for vertically incident PCRs (solid, blue line) and for PCRs incident within an acceptance cone of $70^\circ$ (dashed, orange line). . . . .	23
1.18	Muon spectrum for the typical GCR flux and during GLEs, calculated using the MAIRE tool. . . . .	24

1.19	The anti-correlation between CR count rates and the atmospheric pressure. (a) shows the CR and the local atmospheric pressure measured at a NM in the South Pole; (b) shows the CR and pressure measured by HiSPARC station 501. . . . .	26
1.20	The barometric coefficient calculation: (a) during November 2017 for the South Pole (SOPO) NM station, (b) during November 2019 for HiSPARC station 501 at Nikhef. . . . .	27
1.21	A comparison between the monthly barometric coefficient computed in this work and using the online barometric coefficient tool throughout the year 2017 for the SOPO NM station. . . . .	28
1.22	Pressure corrected HiSPARC data for 2 stations around the epoch of GLE 71. The top panel of each subplot shows the minute-averaged trigger events between detectors within the station, while the bottom panel shows the mean-shifted, minute-averaged counts by each individual detector in the station. The vertical red, dashed line depicts the approximate onset time of the GLE. . . . .	30
1.23	Pressure corrected HiSPARC data for 2 stations around the epoch of GLE 72. The top panel of each subplot shows the minute-averaged trigger events between detectors within the station, while the bottom panel shows the mean-shifted, minute-averaged counts by each individual detector in the station. The vertical red, dashed line depicts the approximate onset time of the GLE. . . . .	31
1.24	HS 8001 (Eindhoven) . . . . .	31
1.25	HS 501 (Nikhef) . . . . .	32
1.26	Pressure corrected HiSPARC data for 2 stations in an epoch where there were two FDs close to the onset of GLE 72. The top panel of each subplot shows the minute-averaged events data, while the bottom panels show the mean-shifted, minute-averaged counts by each individual detector in the stations. The vertical blue-dashed lines show the approximate onset-times of the FDs and the red-dashed line depicts the approximate onset-time of the GLE. . . . .	32
2.1	Schematic diagram of the HiSPARC station 14008 detector set-up. . . . .	35
2.2	HiSPARC 14008 assembly and configuration. (a) shows the stacked arrangement of the scintillators on the lab work bench, between layers of protective foam. (b) shows the complete detector inside the ski-box on the University of Birmingham campus. . . . .	36
2.3	Voltage calibration curve for the PMTs of station 14008. The upper, red-dashed line indicates the upper limit for the low threshold singles rate (400 Hz), and the lower 2, black-dashed lines indicate the upper and lower bounds for the high threshold singles rate (100–130 Hz). . . . .	37
2.4	Schematic diagram of the DS18B20 temperature sensor circuit, whereby the voltage, ground, and GPIO interfaces connect directly into pins of the Raspberry Pi board. . . . .	38

# List of Tables

1.1	Properties of some of the HiSPARC stations: geographic longitude ( $\lambda$ ), geographic latitude ( $\phi$ ), altitude ( $h$ ), and the geomagnetic vertical cut-off rigidity ( $R_C$ ) calculated from the PLANETOCOSMICS simulations. . . . .	11
1.2	Space weather events investigated within the HiSPARC data. The percentage change column provides a reference of how much the CR counts observed by the NM station at Oulu ( $R_c=0.81$ GV) increased or decreased by, due to the space weather event. More precise times for the event onset can be found at NMDB (2018) (for GLEs) and Lingri et al. (2016) (for FDs). . . . .	13
1.3	.....	25
A.1	Details of the proton-initiated air showers simulated using CORSIKA. . . . .	42
A.2	Details of the $\alpha$ -particle-initiated air showers simulated using CORSIKA. . . . .	43

# List of Abbreviations

- AMS-02** Alpha Magnetic Spectrometer.
- AVD** Asymptotic Viewing Direction.
- CORSIKA** Cosmic Ray Simulations for Kascade.
- CR** Cosmic Ray.
- EAS** Extensive Air Shower.
- FD** Forbush Decrease.
- GCR** Galactic Cosmic Ray.
- GLE** Ground Level Enhancement.
- IGRF** International Geomagnetic Reference Field.
- ISS** International Space Station.
- MAIRE** Model for Atmospheric Ionising Radiation Effects.
- MD** Muon Detector.
- MIP** Minimum Ionising Particle.
- MPV** Most Probable Value.
- NM** Neutron Monitor.
- NMDB** Neutron Monitor Data Base.
- PCR** Primary Cosmic Ray.
- PMMA** Polymethylmethacrylate.
- PMT** Photo Multiplier Tube.
- SCR** Solar Cosmics Ray.
- SEP** Solar Energetic Particle.
- UHECR** Ultra-High Energy Cosmic Ray.

# 1 HiSPARC as a Space Weather Detector

## 1.1 Introduction

... [on daily variations (DV)] Dr. Rolf Butikofer (in a reply from Danislav Sapundzjiev, dasapund@meteo.be) said:

*"The daily cosmic ray variation near Earth is caused by the anisotropy of the cosmic ray intensity in the interplanetary space. Cosmic ray particles follow the field lines of the interplanetary magnetic field when they travel towards the interior of the heliosphere. Because of the rotation of the Earth, the angle between the asymptotic cone of acceptance of various energies at the location of ground-based cosmic ray detectors (neutron monitors) and the direction of the interplanetary magnetic field varies with a time period of 24 hours. As a consequence cosmic ray detectors look in different directions in the course of a day and observe therefore a diurnal variation. The daily variations of neutron monitors is mainly seen by high latitude stations which have asymptotic directions at low energies (rigidities) near the equator."*

... [on cosmic ray electron (CRE) losses and lower than protons] Tinivella (<http://arxiv.org/abs/1610.03672>) said:

*"The first term describes ionization losses in ISM and is dominant for energies up to a few tens of MeV. The second term is due to bremsstrahlung, adiabatic losses and pair production in electron-gamma interaction, while the last term represents losses by synchrotron emission and Inverse Compton scattering (IC) under the Thomson approximation, that holds very well for electrons up to a few TeV of energy."*

### 1.1.1 Space Weather Effects

Put something in here about the type of effects that have been observed, and how/why to refer back to with our observations...

### 1.1.2 HiSPARC Project

HiSPARC stands for *High School Project on Astrophysics and Research with Cosmics*, and it is a scientific outreach project that was initiated in the Netherlands in 2002 (Bartels, 2012). The HiSPARC project has two main goals: the study of Ultra-High Energy Cosmic Ray (UHECR) for astroparticle physics research, and to serve as a resource to expose high school students to scientific research (Bartels, 2012).

HiSPARC is a global network of muon detectors spread across the Netherlands, Denmark, the UK, and Namibia. The detectors at each station record muon counts and may be used for many scientific experiments, such as: reconstruction of the direction of a cosmic ray induced air shower, reconstruction of the energy of the air shower's primary particle, investigation between the atmospheric conditions and the number of cosmics rays observed, etc.

Data recorded by the HiSPARC stations are stored and are available publicly at <http://www.hisparc.nl>, where the Cosmic Ray (CR) counts, atmospheric data, station metadata, and more can be found.

### 1.1.3 HiSPARC Detector and Station Configuration

The detection philosophy of HiSPARC is to sample the footprints of Extensive Air Showers (EASs) using coincident triggers between scintillation detectors. As HiSPARC was set up as an outreach programme for high schools, this impacted detector design. Resources are limited in schools and the detectors are usually financed by the participating high schools, colleges, and universities. In addition, students (accompanied by their teachers and local node support staff) are responsible for assembly and installation their detectors, which are typically installed on the roofs of schools.

Due to this, the detectors needed to be cheap, robust, and easily maintainable, therefore the scintillation detector was selected for the HiSPARC network.

Scintillators consist of materials that emit light when charged particles pass through them with sufficient energy to ionise the scintillator material. The total light produced is proportional to the number of charged particles, and can be collected by a Photo Multiplier Tube (PMT). Each HiSPARC detector utilises a plastic scintillator of dimensions 1000 mm x 500 mm x 20 mm, providing a detection area of 0.5 m<sup>2</sup>. A vertically incident Minimum Ionising Particle (MIP) has a most probable energy loss in 2 cm of the scintillation material of 3.51 MeV ( $\equiv$  1 MIP) (van Dam et al., 2020).

The scintillator is glued to a triangular/‘fish-tailed’ light-guide (dimensions, base: 500 mm; top: 25 mm; height: 675 mm), and a light-guide adapter provides the optical interface between the square end of the light-guide and the cylindrical aperture of the PMT. The configuration of a single HiSPARC detector is shown in Figure 1.1.

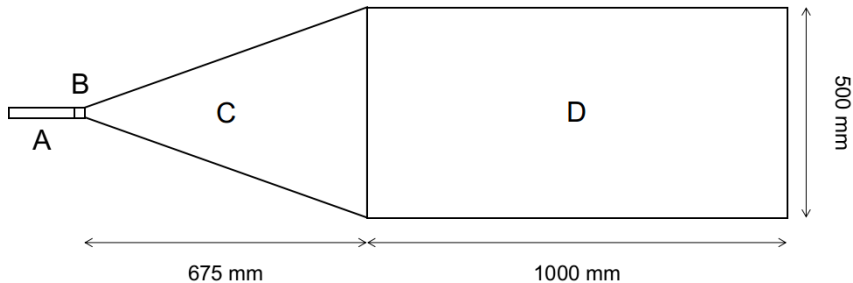


Figure 1.1: Schematic diagram of the HiSPARC scintillation detector. (A): PMT; (B): light-guide adaptor; (C): light-guide; (D): scintillator.

The scintillator is made of a material consisting of polyvinyltoluene as the base, with anthracene as the fluor, and the emission spectrum peaks at a wavelength of 425 nm (Fokkema, 2012; Bartels, 2012). The light-guide is made from Polymethylmethacrylate (PMMA) and has a comparable refractive index to the scintillator (1.58 and 1.49, respectively), reducing refraction effects between the two materials (van Dam et al., 2020).

The PMT used is an ETEEnterprises 9125B PMT, with a 25 mm aperture, blue-

green sensitive bialkali photocathode, and 11 high-gain dynodes (Bartels, 2012; ETEEnterprises, 2020). The quantum efficiency of the PMT used in the HiSPARC detectors peaks at around 375 nm at 28%, and at 425 nm the quantum efficiency is 25% (Fokkema, 2012).

Each detector is wrapped in aluminium foil (thickness 30  $\mu\text{m}$ ) and a black, vinyl material (thickness 0.45 mm), which is usually used as a pond liner, to ensure light-tight detectors and to reduce the noise level from stray photons (van Dam et al., 2020). In addition, each detector is placed inside of its own a plastic ski-box to again ensure that it is light-tight, and to also ensure that it is weather-proof, as the detectors are usually located on the roofs of schools, colleges, and universities.

A HiSPARC station combines either 2 or 4 detectors, to observe coincident muons ('events'), and typical configurations of each are shown in Figure 1.2. The separation between detectors varies from station-to-station. In addition some stations have the capability to measure the local atmospheric properties, such as temperature, pressure, relative humidity etc. Moreover, some stations also record the 'singles' rates, i.e. the frequency at which an individual detector is triggered, independently of the other detectors in the station. The singles rates are important when investigating non-EAS events.

light pulse which is converted into an electric pulse by the PMT. This pulse is sampled and digitized at 400 MHz

The PMTs of the detector in a station are connected to HiSPARC electronics boxes, which sample and digitise the signal at a rate of 400 MH, and each PMTs is connected to the electronics box using cables of a standard length of 30 m, to minimise any timing offsets between detectors (Fokkema, 2012; van Dam et al., 2020). The electronics boxes are capable of controlling and reading two PMTs, therefore a four-detector station requires two electronics boxes: a master and a slave.

The HiSPARC experiment is set up in such a way as to ensure that each station



(a) Two-detector station configuration



(b) Four-detector station configuration (triangle arrangement)



(c) Four-detector station configuration (diamond arrangement)

Figure 1.2: Typical formations of two-detector and four-detector stations. In each, the grey circle denotes a GPS antenna which is located in between the detectors to provide a precise timestamp for each signal.

across the HiSPARC network reads a similar count rate of muons, in order to aid the direct comparison between the different stations in the network. When configuring the station, a trigger threshold must be applied for the PMT signals. This is

standardised across the HiSPARC network and can be seen in relation to a detector trigger pulse in Figure 1.3a. There are two thresholds, low: 30 mV, which represents 0.2 of a MIP; high: 70 mV, which represents 0.5 of a MIP (Fokkema, 2012; van Dam et al., 2020). The thresholds were chosen to increase the sensitivity of the stations for observing gamma rays and low energy electrons, but this has the effect of making it more difficult to determine whether an individual detection is from a muon, or another MIP. This is why the HiSPARC network usually relies on detecting ‘events’, from coincident muons.

Each detector in the network is set up such that the pulseheight spectrum peaks at a Most Probable Value (MPV) of  $\sim 150$  mV (see Figure 1.3), and such that the high threshold allows a mean count rate on the order 100 counts per second and the low threshold allows a mean count rate of the order 400 counts per second; these can be tuned by adjusting the PMT voltage. It could be argued that in setting up the detectors in this way, there is an immediate bias in the data to reject lower energy CRs.

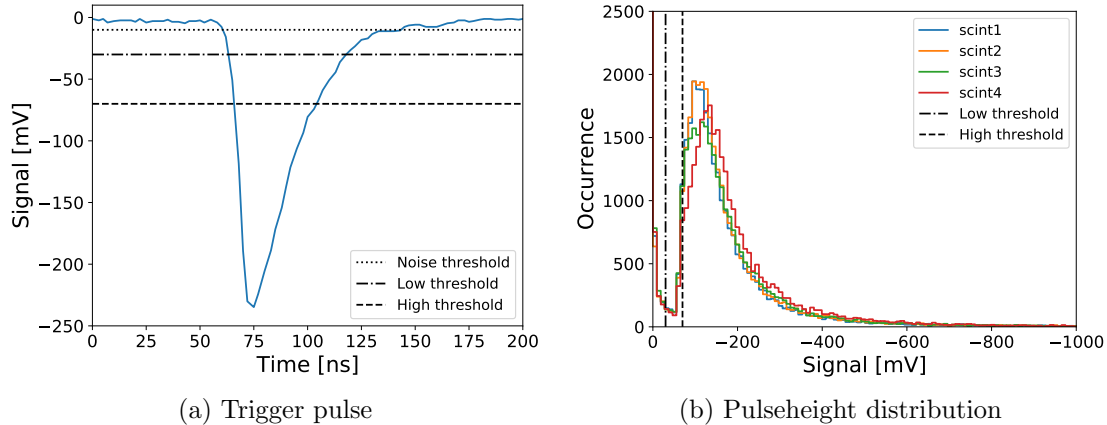


Figure 1.3: (a): An example PMT signal after digital conversion by the HiSPARC electronics box. The horizontal lines denote: the noise cut-off (dotted line), which is used for setting a limit when integrating the pulse height, to give the pulse integral; the low-voltage threshold (dash-dot); the high-voltage threshold (dashed). (b) The pulse height distribution over the course of a single day from HiSPARC station 501. The vertical lines show the low-voltage threshold (dash-dot) and the high-voltage threshold (dashed).

The pulse height spectrum (see Figure 1.3b) is composed of two main regions:

the left side which falls off rather steeply and the main, asymmetric part of the spectrum which features a peak and a long tail. The left side of the spectrum is understood to be from high-energy photons (gamma rays) produced in air showers (Fokkema, 2012). These high-energy photons may undergo pair production when interacting with the scintillator which may produce ionising electron and positron pairs. The trigger thresholds are placed to reject these noise signals from the data.

The main, asymmetric distribution which features a peak and a tail is from charged particles (muons and electrons) (van Dam et al., 2020). The mean energy loss of particles in a material is described by the Blethe-Bloch formula; however this does not account for fluctuations in energy loss (Fokkema, 2012). A Landau distribution in fact describes the fluctuations in energy loss of particles. Due to the resolution of the HiSPARC detectors the distribution in Figure 1.3b is best described by the convolution of the Landau distribution with a normal distribution which describes the resolution of the detector (Fokkema, 2012). The peak of the distribution, the most probable values (MPV), is the most likely energy lost by a particle in the detector, i.e. the 3.51 MeV MIP (van Dam et al., 2020). It has been shown that the location of the MPV can vary due to the effects of atmospheric temperature (Bartels, 2012; van Dam et al., 2020).

The default trigger conditions for detecting an air shower event between multiple PMTs within a station differ for a two/four-detector station. In a two-detector station, an event is recorded if the PMT signals from both detectors exceed the low threshold within the coincidence time window ( $1.5\ \mu s$ ). In a four-detector station, there are two conditions: (i) at least two detectors exceed the high threshold within the coincidence time window; (ii) at least three detectors exceed the low threshold within the coincidence time window. These are the default conditions, but there are other, user configurable ways of triggering the station.

The scientific goals that can be achieved also vary between the two/four-detector stations. When at least three detectors in a four-detector station observe particles of

an EAS, the direction of the EAS (and thus the direction of the Primary Cosmic Ray (PCR)) can be acquired using triangulation calculations. When only two detectors in a station observe particles of an EAS, i.e. the limit for a two-detector station, it is only possible to reconstruct the arrival direction along the axis that connects the centres of those two detectors (thus it is not possible to reconstruct the direction of the PCR).

## 1.2 Aims

The HiSPARC project was set up with the detection philosophy of observing EAS, which are typically associated with PCRs with energy of  $\sim 10^{14}$  eV and above, that produce large footprints observable with many HiSPARC stations simultaneously. For PCRs with energy below  $\sim 10^{14}$  eV the air shower is small, with almost no observable muon footprint, and for PCRs with energy below  $\sim 10^{11}$  eV, there is typically fewer than one or two muons that reach the ground, making their observation difficult. Most muons produced by such low-energy PCRs decay higher in the atmosphere and their energy is mostly transferred into the resultant electron (van Dam et al., 2020), which is observable by HiSPARC.

The HiSPARC detectors are capable of observing any muons that reach them, therefore the project was motivated by the existing network of Muon Detector (MD) which may have the capability of observing the CRs associated with space weather events.

The principle aim of the project was to determine whether the existing HiSPARC network is capable of observing space weather events. To do this, we investigated the properties of the HiSPARC detectors, to learn about what typical PCRs we observe. This was initially achieved by investigating the data during periods of space weather activity to search for the associated signatures. We searched through some of the most reliable HiSPARC stations to determine whether these events were observed in the data. This was done to determine whether, without much effort, we could get

a binary answer on whether these events were observed by HiSPARC.

Following this, we performed simulations of air showers initiated by CRs to understand the expected muon flux and dispersion at ground level. This helped us to understand how likely it is to observe the PCRs associated with space weather with the HiSPARC detectors, observing muons.

Finally, ground-based observations of muons from air showers are susceptible to the conditions in the atmosphere; therefore, where possible, we corrected for atmospheric effects and again reviewed the corrected data to determine whether the space weather events were observed.

### 1.3 HiSPARC Properties

To understand the PCR spectrum that the HiSPARC stations are capable of observing, PCR transport simulations were performed using the PLANETOCOSMICS software. PLANETOCOSMICS performs Geant4 Monte Carlo simulations of charged particle transport through Earth’s magnetosphere based on Størmers transport equation for charged particles (Desorgher et al., 2006). PLANETOCOSMICS simulates backward trajectories of charged particles from a given location (latitude, longitude, and altitude) out to the magnetopause for a set of PCR rigidities.

For each trajectory there are two possible outcomes: (i) the particles trace out to the magnetopause where they escape Earth’s magnetosphere, an allowed trajectory; (ii) the particles are sufficiently bent by the effect of the Earth’s magnetosphere that they do not reach the magnetopause and cannot escape the Earth’s magnetosphere, a forbidden trajectory (Desorgher et al., 2006). The coordinates of the asymptotic direction at the magnetosphere are provided as an output to the simulations projected back down to the Earth’s surface. In this work PLANETOCOSMICS was configured with the Tsyganenko-89 model for the external magnetospheric magnetic field and the International Geomagnetic Reference Field (IGRF) internal field model.

For each rigidity simulated, whether it was an allowed or forbidden trajectory was stored, which was used to provide an insight into the rigidity spectrum for a given station. From the allowed trajectories the effective cut-off rigidity ( $R_C$ ) for the stations was computed using equation (1.1), where  $R_U$  is the upper rigidity (the last allowed trajectory before the first forbidden trajectory);  $R_L$  is the lower rigidity (the last allowed trajectory before which all other trajectories with a lower rigidity are forbidden);  $\Delta R$  is the rigidity step size in the simulation (Desorgher et al., 2006; Herbst et al., 2013).

$$R_C = R_U - \sum_{i=R_L}^{R_U} \Delta R_i \quad (1.1)$$

The rigidity spectrum for each of the HiSPARC stations were investigated to determine  $R_C$  for each station. The cut-off rigidity calculated for the six HiSPARC stations for a vertical incidence upon the atmosphere (i.e.  $0^\circ$  zenith angle) are shown in Table 1.1 which show that there is little variation in  $R_C$  between the HiSPARC stations and that they observe protons with rigidities in excess of  $\sim 3$  GV. This analysis was initially carried out for the vertical direction (i.e. azimuth =  $0^\circ$ , zenith =  $0^\circ$ ); however further trajectories were simulated for different azimuth and zenith angles to determine the dependence of the rigidity spectrum on the detector acceptance angle. The analysis for the azimuthal dependence was carried out at a zenith angle of  $20^\circ$  as this is around the most probable angle for HiSPARC events, and the analysis of the zenith dependence was carried out at an azimuth angle of  $0^\circ$ .

The small variation between HiSPARC stations is due to their close proximity in geographic latitude and longitude. The values of  $R_C$  calculated for the HiSPARC stations suggest that they should be able to observe higher energy Solar Cosmics Ray (SCR), but may not be as susceptible as the higher latitude Neutron Monitor (NM) where the effects of Ground Level Enhancements (GLEs) are highly observable.

As a results of the PLANETOCOSMICS simulations it was possible to under-

Table 1.1: Properties of some of the HiSPARC stations: geographic longitude ( $\lambda$ ), geographic latitude ( $\phi$ ), altitude ( $h$ ), and the geomagnetic vertical cut-off rigidity ( $R_C$ ) calculated from the PLANETOCOSMICS simulations.

Station Name/ID	$R_C$ [GV]	$\lambda$ [deg]	$\phi$ [deg]	$h$ [m]	No. Detectors
Nikhef/501	3.19	4.95 E	52.36 N	56.18	4
College Hageveld/203	3.18	4.63 E	52.35 N	53.71	2
Leiden/3001	3.23	4.45 E	52.17 N	54.08	2
Eindhoven/8001	3.44	5.49 E	51.45 N	70.12	2
Birmingham University/14001	3.06	1.93 W	52.45 N	204.14	4

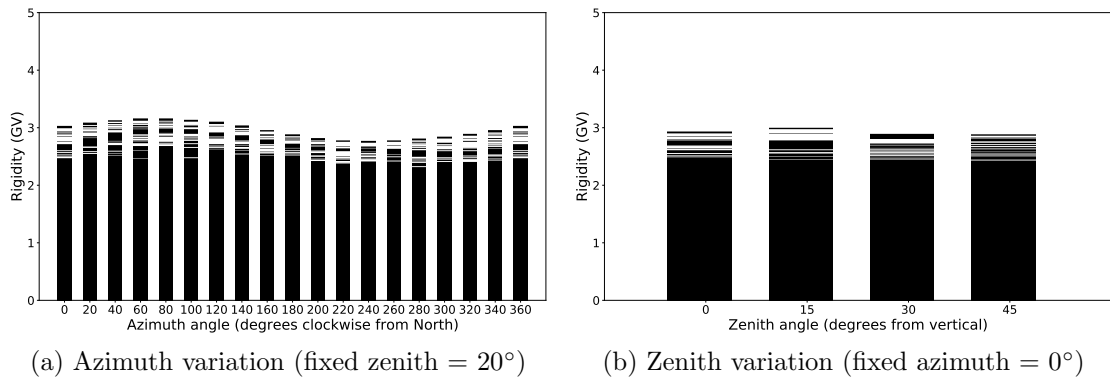


Figure 1.4: Azimuthal and zenith angle variations in the allowed and forbidden rigidity trajectories for HiSPARC station 501.

stand the trajectories of particles that enter the Earth's magnetosphere prior to arrival at the atmosphere. It can be seen from Figure 1.5 that the Asymptotic Viewing Directions (AVDs) for each of the HiSPARC stations investigated are rather similar, and that they mostly straddle the equator for low rigidity PCRs.

The simulations were only performed up to a rigidity of 20 GV; however, at higher rigidities, we would see the AVDs spiral in towards the geographic location of the station, and the PCR would enter the magnetosphere and atmosphere almost vertically above the detector. This map of the AVDs also informs us that we should expect to be able to observe some lower energy PCRs when the zenith of the detector is not facing the asymptotic direction of the PCR.

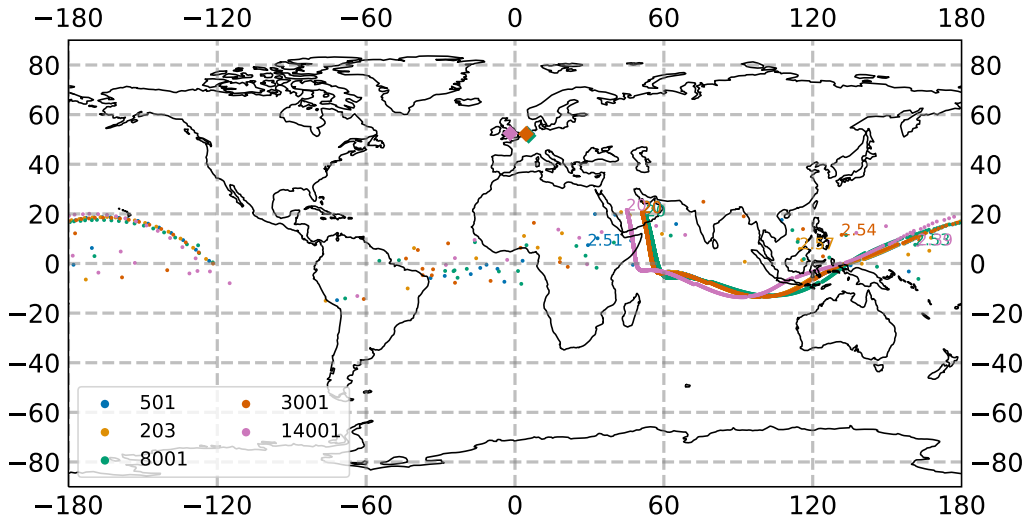


Figure 1.5: The vertical asymptotic viewing directions of 5 HiSPARC stations. The rigidity range of the simulations were from  $1.0 \text{ GV} < R < 20.0 \text{ GV}$ , and the results are plotted in geographic coordinates on January 20th 2005. The diamonds correspond to the HS ground location and the circles correspond to the AVD for a specific rigidity value.

## 1.4 HiSPARC Observations

[...!!...end with discussion on unknown PCRs observable and the effect of atmospheric weather conditions that need to be accounted for...]

The effects of space weather on CRs has been outlined in [REF intro]. It was highlighted during private communication with the UK Met Office that observations of GLEs are of more interest and importance to space weather forecasts and nowcasts. Forbush Decreases (FDs) are of lower interest and importance, we still searched for FDs within the HiSPARC data. Table 1.2 outlines the specific space weather driven GLEs and FDs that we searched for within the HiSPARC data.

The specific events in Table 1.2 were selected as: (i) for the GLEs, they are the only three that fall in the HiSPARC operational period; (ii) for the FDs, they are the only individual, or set of, FDs that result in a count variation in excess of  $\sim 5\%$  and the largest FDs are likely to be the most promising candidates for observation with HiSPARC.

For comparison with the HiSPARC results shown below, we show the GLEs, as

Table 1.2: Space weather events investigated within the HiSPARC data. The percentage change column provides a reference of how much the CR counts observed by the NM station at Oulu ( $R_c=0.81$  GV) increased or decreased by, due to the space weather event. More precise times for the event onset can be found at NMDB (2018) (for GLEs) and Lingri et al. (2016) (for FDs).

<b>GLE Onset</b>	<b>GLE</b>	<b>% Change (Oulu)</b>	<b>FD Onset</b>	<b>% Change (Oulu)</b>
13/12/2006	70	~ 90%	08/03/2012	~ 10%
17/05/2012	71	~ 15%	12/03/2012	~ 3 – 5%
10/09/2017	72	~ 5%	14/07/2012	~ 3%
			21/12/2014	~ 5%
			06/09/2017	~ 2%
			07/09/2017	~ 8%

observed by the Oulu NM station, in Figure 1.6. It is clear from Figure 1.6 that the relative increase of the GLEs was large for GLE 70 and 71, but much more subtle for GLEs 72. We expect that if we are to observe any of the GLEs, we shall have the best chance of observing GLEs 70.

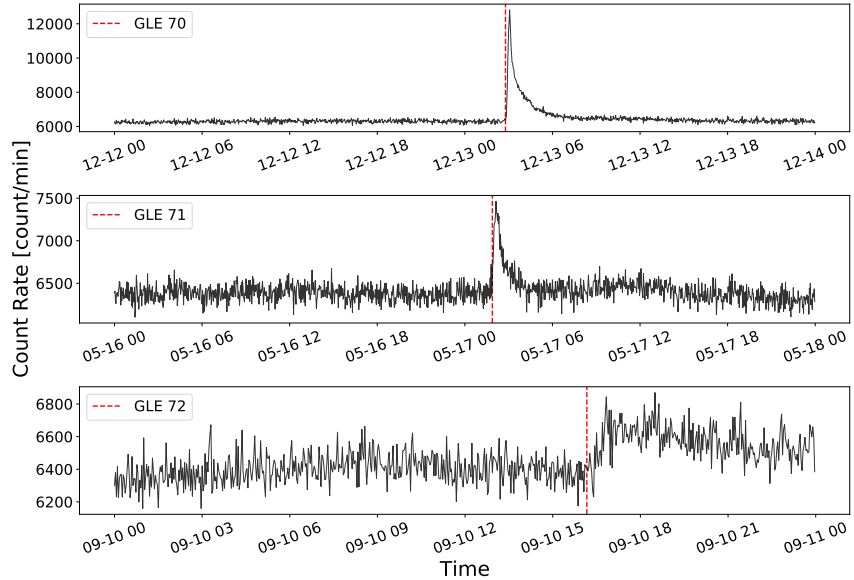


Figure 1.6: GLEs observed by the NM stations based at Oulu. Top panel: GLE 70; middle panel: GLE 71, bottom panel: GLE 72. The solid-black line shows the 2-minute-averaged, pressure corrected data and the vertical, dashed-red lines show the epochs of each GLE onset.

Similarly, we show a comparison plot for the FDs, as observed by the Oulu NM station, in Figure 1.7.

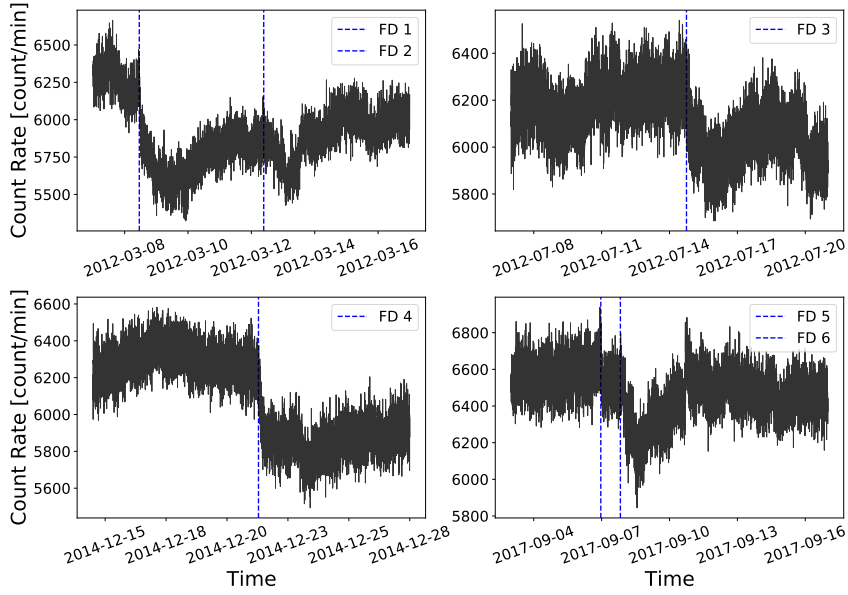


Figure 1.7: FDs observed by the NM stations based at Oulu. Top left panel: FDs during March 2012; top right panel: FD during July 2012, bottom left panel: FD during December 2014; bottom right panel: FD during September 2017. The solid-black line shows the 2-minute-averaged, pressure corrected data and the vertical, dashed-blue lines show the epochs of each FD onset.

As there are only a few space weather events that we were particularly interested in, and only a few HiSPARC stations that we felt were reliable for our investigation, we conducted the search for these GLEs and FDs by-eye in the data .

#### 1.4.1 HiSPARC Observations of Ground Level Enhancements

The search for evidence of GLEs within the HiSPARC data was conducted for GLE 70, 71, and 72, as they are the only GLEs that span the operational epoch of the HiSPARC network. Figure 1.8, Figure 1.9, and Figure 1.10 shows the HiSPARC observations around the epochs of GLE 70, 71, and 72, respectively.

Most of the observations show only the HiSPARC events data (i.e. coincidences between the detectors of a station); however, where possible, we also show the singles rates from each of the individual detectors in a station when the singles rate data is available.

We can see from Figures 1.8, 1.9, and 1.10 that there are no clear and obvious signs of the GLE signals in the HiSPARC observations. This is the case for both

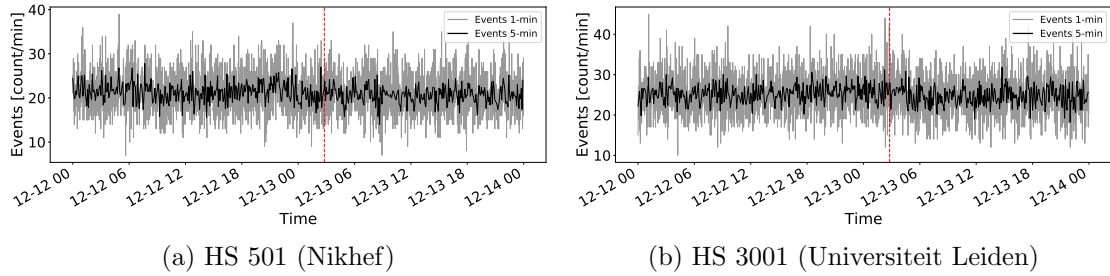


Figure 1.8: HiSPARC data for stations 501 and 3001 around the epoch of GLE 70. The plot shows the minute-averaged and 5-minute-averaged trigger events between detectors within the station. The vertical red, dashed line depicts the approximate onset time of the GLE. The units of time on the x-axis are, MM-DD HH.

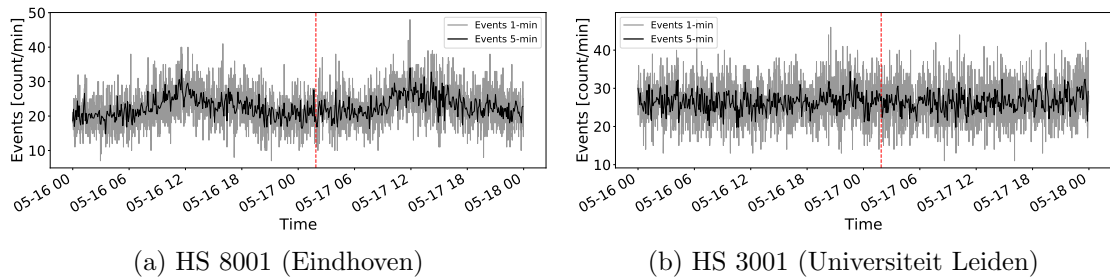


Figure 1.9: HiSPARC data for stations 8001 and 3001 around the epoch of GLE 71. The plot shows the minute-averaged and 5-minute-averaged trigger events between detectors within the station. The vertical red, dashed line depicts the approximate onset time of the GLE. The units of time on the x-axis are, MM-DD HH.

the events data and the singles data.

There are some excursions from the mean count rate, this is significantly more prominent in the singles rates which are shown in the GLE 72 plots for stations 501, 203, and 8001. It is believed that these excursions are the effect of atmospheric pressure on the muon count rates; in Section 1.6 this is discussed further and is accounted for.

No clear GLEs have been observed in the HiSPARC data. We believe this is due to the rigidity cut-off of the HiSPARC stations, as GLEs are caused by Solar Energetic Particles (SEPs) with a lower energy. Typically GLEs are observed by NMIs, and only the most energetic have been observed by MDs [...](...cite to <https://doi.org/10.1088/0004-637X/761/2/101> and maybe also to <https://doi.org/10.1093/pasj/psv1>). In Section ?? we investigated the CR spectrum to infer our ability to measure GLEs

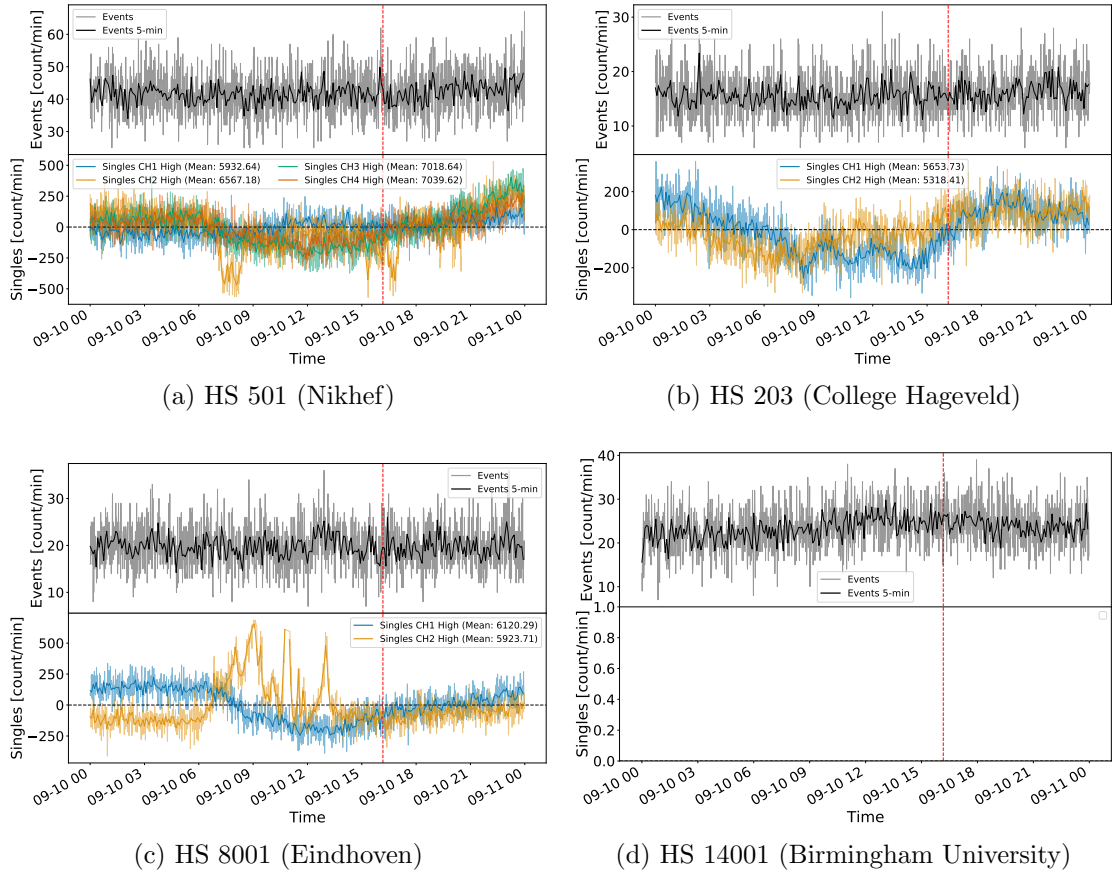


Figure 1.10: HiSPARC data for 4 stations around the epoch of GLE 72. The top panel of each subplot shows the minute-averaged trigger events between detectors within the station, while the bottom panel shows the mean-shifted, minute-averaged counts by each individual detector in the station. The vertical red, dashed line depicts the approximate onset time of the GLE. The units of time on the x-axis are, MM-DD HH.

with the HiSPARC stations. We do also note that the atmospheric effects in the raw do not help our ability to observe the space weather and these effects were later removed (see Section 1.6.2).

#### 1.4.2 HiSPARC Observations of Forbush Decreases

The search for evidence of FDs within the HiSPARC data was conducted for the FDs highlighted in Table 1.2. Figure 1.11, Figure 1.12, and Figure 1.13 show the HiSPARC observations around the epochs of the first four FDs listed in Table 1.2. Each of the plots shows only observations using the HiSPARC events data (i.e. coincidences between the detectors of a station).

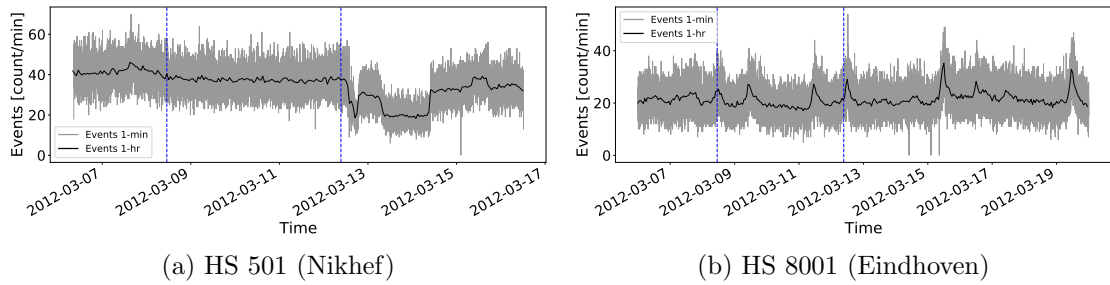


Figure 1.11: HiSPARC data for stations 501 and 8001 around the epoch of the FDs in March 2012. The plot shows the minute-averaged and hourly-averaged trigger events between detectors within the station. The vertical blue-dashed lines show the approximate onset-time of the FDs.

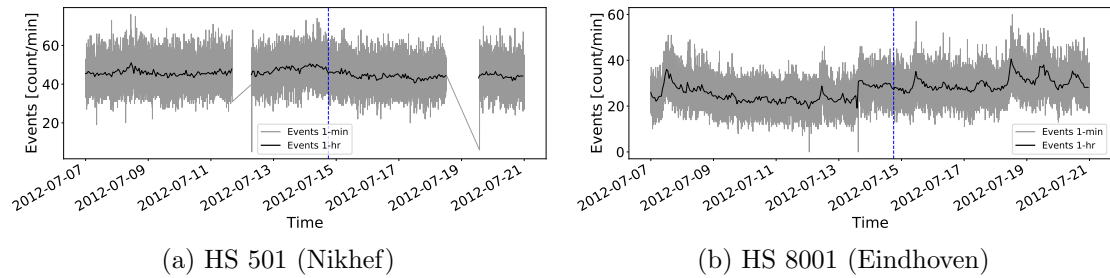


Figure 1.12: HiSPARC data for stations 501 and 8001 around the epoch of the FD in July 2012. The plot shows the minute-averaged and hourly-averaged trigger events between detectors within the station. The vertical blue-dashed line shows the approximate onset-time of the FD.

We can see from the plots that there are no clear signs of the anticipated FD signals in the HiSPARC observations. We observed a set of significant decreases in the muon count rate in station 501 after the second FD in March 2012 (see Figure 1.11a); however, it is unclear whether this is a consequence of the FD or other, hardware reasons, as the FD was not observed in the other HiSPARC station. The shape of the FD in the NM data shows a sudden decrease and a smooth recovery within two days, but the shape of the HiSPARC data shows a more complicated effect, which suggests that the cause is not the FD, but rather a result of hardware.

In the other station we also observe some variations in the count rate which vary over longer time scales, but this is due to variations in the atmospheric pressure. Note that this needs accounting for and comes later...

It is quite clear from Figure 1.11b and Figure 1.12b that stations 8001 (Eind-

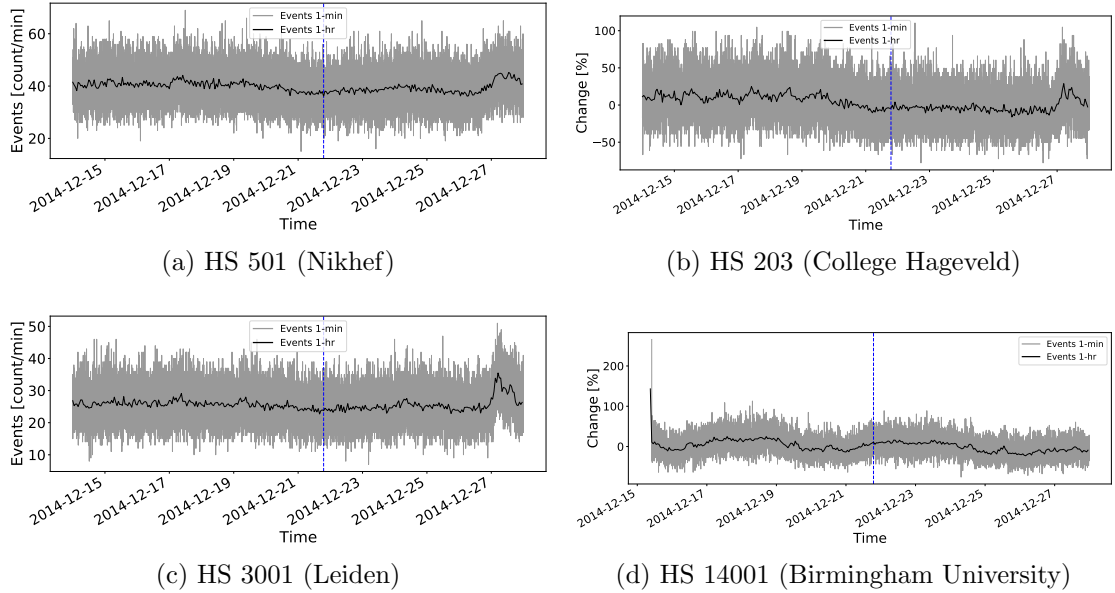


Figure 1.13: HiSPARC data for 4 stations around the epoch of the FD in December 2014. The plot shows the minute-averaged and hourly-averaged trigger events between detectors within the station. The vertical blue-dashed line shows the approximate onset-time of the FD.

hoven) displays a semi-persistent diurnal variation in the count rate...

For the final two FDs listed in Table 1.2, the plot of the HiSPARC observations is shown in Figure 1.14. Plotted are the HiSPARC events data, and where possible, we also show the singles rates from each of the individual detectors in a station when the singles rate data is available. Furthermore, as these FDs were precursory to GLE72, we also marked on the epoch of the GLE for completeness.

As with the other FD epochs, we again do not observe any clear signs of the FD signals in either the events or singles data. In each of the three stations for which there was singles data, we observed the semi-persistent diurnal signal, and again in the events for stations 14001. Furthermore, we also observed a similar slower variation in the count rate which is due to atmospheric pressure and needs to be accounted for.

No clear signal of FDs has been observed in the raw HiSPARC data. We again believe this could be due to the rigidity cut-off of the HiSPARC stations. We also note that the atmospheric effects in the raw do not help our ability to observe the

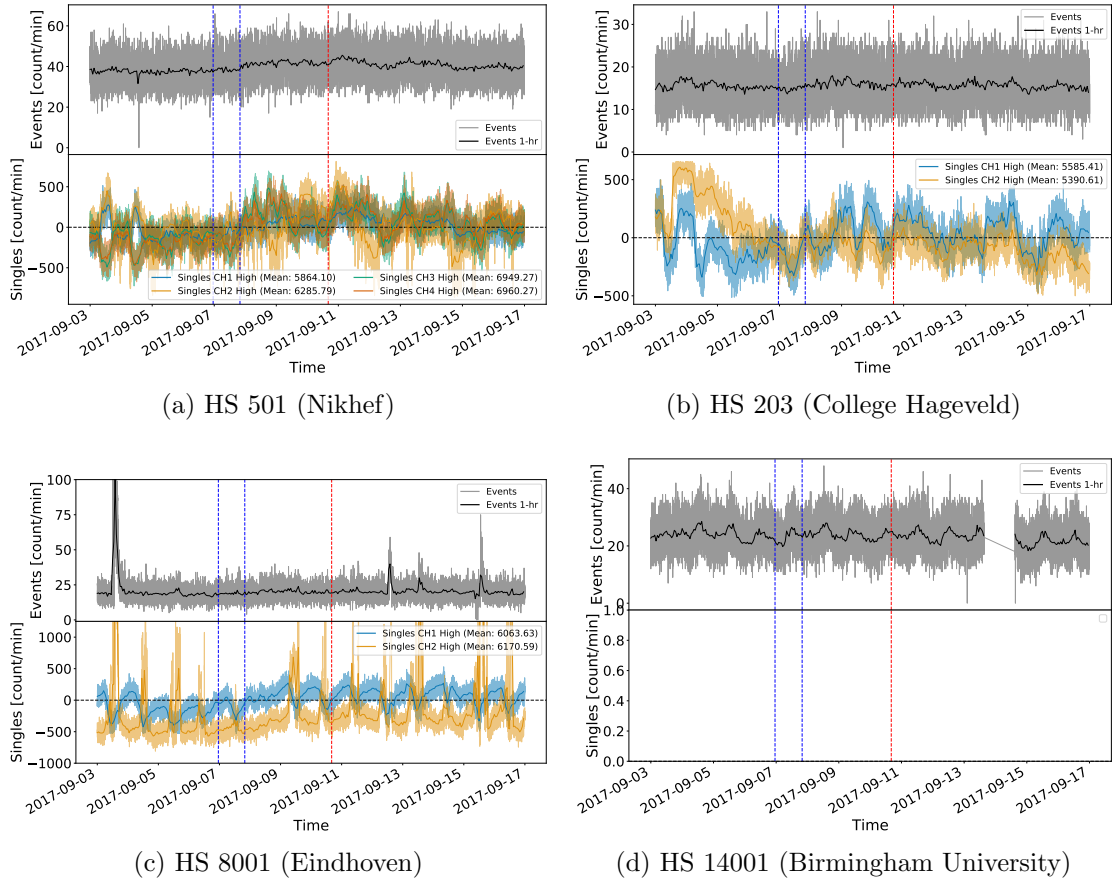


Figure 1.14: HiSPARC data for [n] stations around the epoch in which there were several FDs close to the onset of GLE 72. The top panel of each subplot shows the minute-averaged trigger events between detectors within the station, while the bottom panel shows the mean-shifted, minute-averaged counts by each individual detector in the station. The vertical blue-dashed lines show the approximate onset-times of the two FDs observed around this epoch and the red-dashed line depicts the approximate onset time of the GLE.

space weather and these effects were later removed (see Section 1.6.2).

## 1.5 Air Shower Simulations

In order to understand the muon abundance and the scale of the footprints of air showers produced by PCRs, simulations of air shower developments were performed for a range of PCRs energies for both primary protons and  $\alpha$ -particles.

To simulate the CR air shower development, the Cosmic Ray Simulations for Kascade (CORSIKA) software was employed: a Monte Carlo programme providing detailed simulations of the evolution of air showers initiated by PCRs through the

atmosphere (Heck & Pierog, 2017). The particles in the CORSIKA simulations are tracked through the atmosphere until they undergo interactions with atmospheric nuclei, decay due to their instability, or reach the ground level defined as the simulation terminator.

Proton and  $\alpha$ -particle initiated air showers were generated with energies ranging from  $10^9$  to  $10^{20}$  eV, and  $4 \times 10^9$  to  $10^{20}$  eV, respectively. In total  $\sim 2 \times 10^5$  proton-initiated showers were simulated and  $\sim 2 \times 10^5$   $\alpha$ -particle-initiated air showers were simulated. The lists detailing the breakdown of PCR energies and number of simulations is provided in Appendix A, along with a brief discussion of the settings chosen within the simulations.

### 1.5.1 Air Shower Footprints

The average footprint of muons at ground level was acquired from the output CORSIKA simulations by taking the distribution of the muons at ground level at the end of the simulation as a function of their distance from the shower core. This was achieved for each individual simulation realisation, and for a given PCR energy, the average footprint distribution was calculated by combining all of the individual simulation realisations. Figure 1.15 shows the distributions for air showers induced by vertically incident protons and  $\alpha$ -particles.

We also repeated the simulations for air showers randomly selected from a uniform distribution of incident angles between  $0^\circ$  (vertical) and  $70^\circ$ , to provide a more representative simulation. Similar plots were produced to those in Figure 1.15, but they are not shown here, as the difference is not drastically different by-eye.

The interpretation of Figure 1.15 provides an understanding of the minimum energy PCRs observable by the different stations within the HiSPARC network. The typical separation between the detectors in a HiSPARC station is  $\sim 10$  m; however, the separation between detectors varies from station-to-station and can be up to as much as some 20 m or as low as just a couple of metres. From the

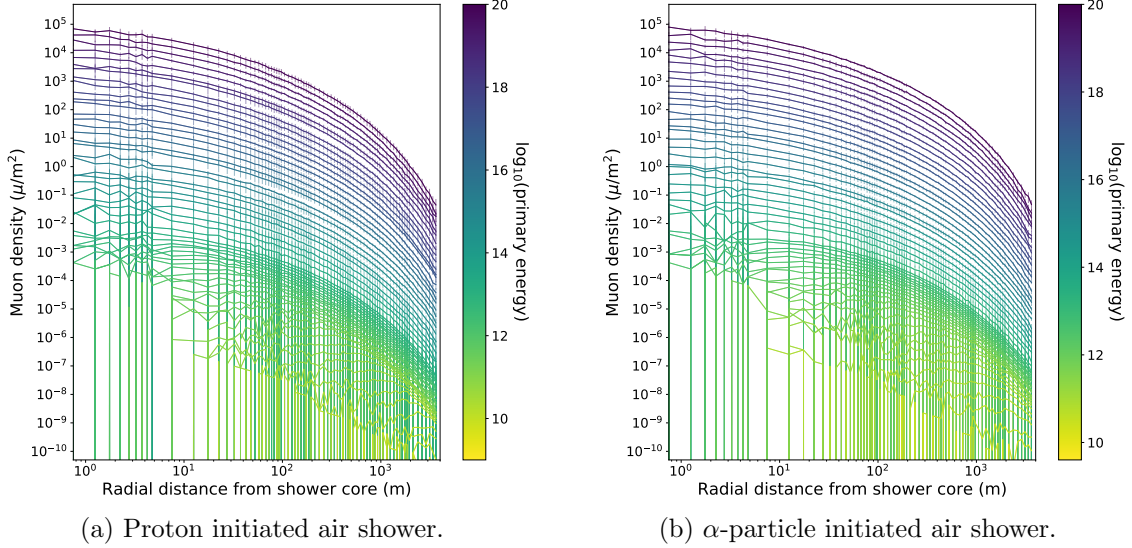


Figure 1.15: Mean muon density footprints for (a) proton-initiated air showers and (b)  $\alpha$ -particle-initiated air showers with initial PCR trajectories with zenith angles  $\theta = 0^\circ$  and various PCR energies. The error bars given represent  $1\sigma$ .

simulations we inferred that the variation in PCR energy sampled varies marginally over this range of detector separations and suggests that HiSPARC stations will typically observe PCRs with an energy on the order of  $\sim 10^{14} - 10^{15}$  eV and above, as they produce a sufficient density of muons to meet the required trigger conditions.

This helps explain why the GLEs and FDs were not observed in the HiSPARC events data. The effects of GLEs and FDs are more prominent at lower PCR rigidities and the air showers induced by the lower rigidity PCR are not sufficient to induce an air shower that will trigger multiple detectors in a station. It was more likely that we may have observed the GLEs or FDs in the singles data, as this only records the count rate of an individual detector, but again they were not observed, which may be explained looking at the flux of the muons at ground level.

### 1.5.2 Muon Flux

From the air shower simulations it was also possible to gain an estimate of how many muons are produced per PCR. Figure 1.16 shows the energy distribution of muons produced per primary PCR, for air showers induced by vertically incident protons

and  $\alpha$ -particles.

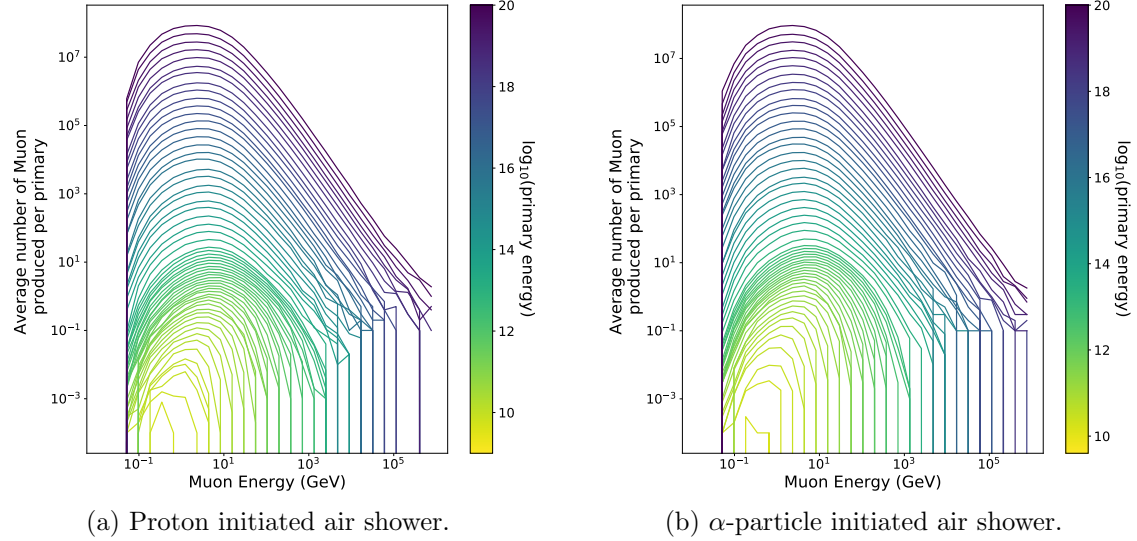


Figure 1.16: Mean number of muons produced at ground level by the PCR for (a) proton-initiated air showers and (b)  $\alpha$ -particle-initiated air showers, for various PCR energy.

The vertically incident air showers provides an upper boundary on the muon flux, but we also repeated the simulations for air showers randomly selected from a uniform distribution of incident angles between  $0^\circ$  (vertical) and  $70^\circ$ , to provide a more representative flux. Similar plots were produced to those in Figure 1.16, but they are not shown here, as the difference is not drastically different by-eye. We see from this analysis that PCRs with an energy less than  $\sim 10^{11} - 10^{12}$  eV produce only one or two muons that reach ground level, and below this PCRs energy, it is rare that any muons are produced.

This helps explain why the GLEs and FDs were not observed in the HiSPARC events data. The effects of GLEs and FDs are more prominent at lower PCR rigidities, i.e. energies  $\gtrsim 10^9$  eV. The air showers induced by the lower rigidity PCRs are not sufficient to produce significant increases in the flux of the muons at ground level.

We also used the data from the simulations to estimate the total muon flux at ground level, based on the PCR flux at the top of the atmosphere. We used a model for the CR flux, taken from Corti et al. (2019), which utilised measurements from the

Alpha Magnetic Spectrometer (AMS-02) on-board the International Space Station (ISS). Figure 1.17 shows the computed differential flux of muons at ground level, based on the simulations of vertically incident PCRs and those randomly simulated within a  $70^\circ$  acceptance cone.

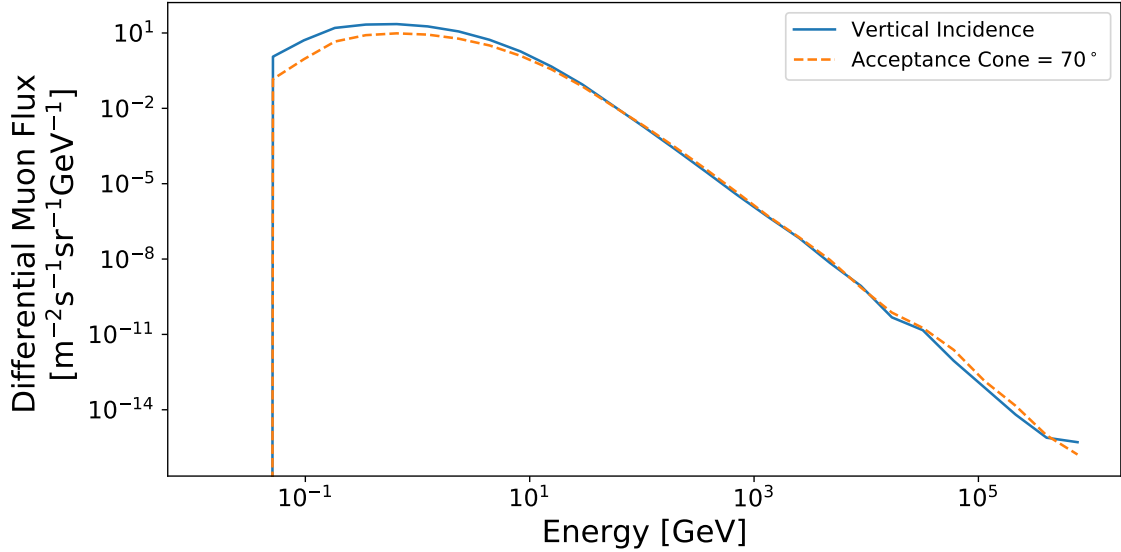


Figure 1.17: Muon differential flux computed using CORSIKA for vertically incident PCRs (solid, blue line) and for PCRs incident within an acceptance cone of  $70^\circ$  (dashed, orange line).

From Figure 1.17, we see that the ground-based flux is similar for both types of simulation performed. In both, the low-energy muon flux dominates, and peak at a muon energy of  $\sim 1$  GeV.

Finally, we used these calculated spectra to determine the expected rate of muons passing through a single HiSPARC detector. We computed the rates as:  $85.365 \mu/\text{s}$  (for non-vertical, i.e.  $70^\circ$  acceptance cone simulations), and  $156.924 \mu/\text{s}$  (for vertical simulations). These rates are comparable to the generally accepted, average ground level muon flux of  $\sim 1$  per  $\text{cm}^2$  per second [cite to Autran: (<https://doi.org/10.1016/j.nima.2018.06.03>)

### 1.5.3 Muon Flux From MAIRE

As a further comparison, we used the online Model for Atmospheric Ionising Radiation Effects (MAIRE) tool to compute the muon spectrum in the atmosphere. MAIRE allows the computation of the secondary particle spectra in the atmosphere,

caused by SEPs. MAIRE has the advantage of also having the PCR spectra for a number of GLEs built in, and therefore we obtained the muon spectra from these a few of the strongest GLEs at the Nikhef HiSPARC station (501). Figure 1.18 shows the muon spectra for a ‘typical’ Galactic Cosmic Ray (GCR) spectrum, and the additional muon spectrum for seven of the largest GLEs to date (which is additive to the GCR spectrum).

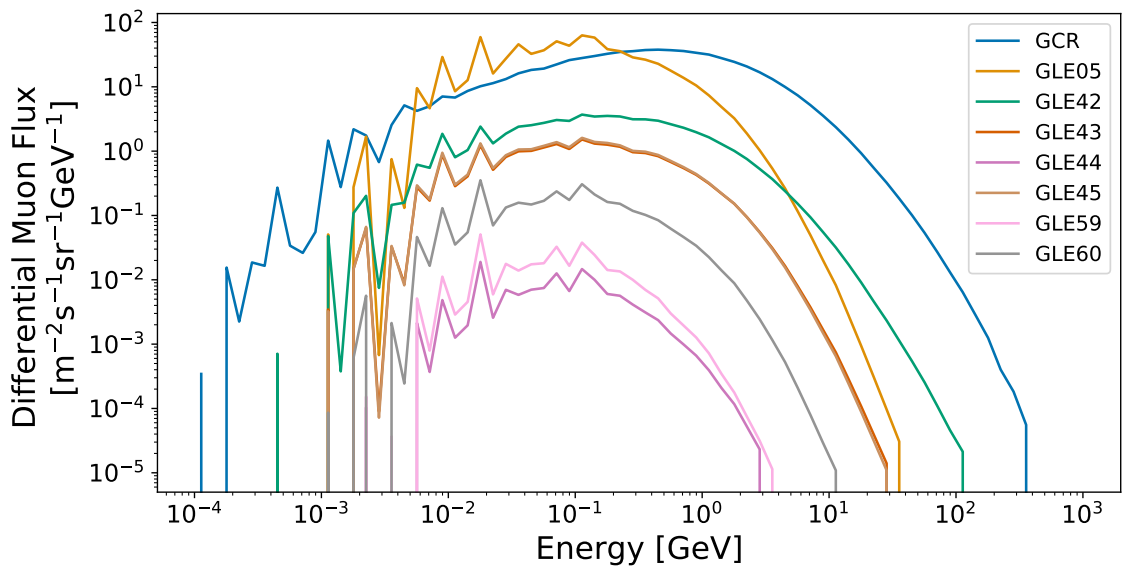


Figure 1.18: Muon spectrum for the typical GCR flux and during GLEs, calculated using the MAIRE tool.

We can see that the GCR-induced muon spectrum in Figure 1.18 roughly agrees with that computed using CORSIKA, which provides confidence in the results of both simulations. We can see that the effect on the muon spectrum drastically varies for the seven GLEs. The maximum increase in the NM count rate for each of the GLEs is summarised in Table 1.3.

The effects of these GLEs are all very large, and the only modern GLE (i.e. in Table 1.2) that is comparable to any of these is GLE 70, which is comparable to GLE 43 and 59. Unfortunately, there are few HiSPARC observations due to the immaturity of the project at the time and we have shown that we do not observe GLE 70 in the HiSPARC data.

The additional contribution from the GLEs is small, and for most of the GLEs,

Table 1.3: ...

GLE	Date	% Peak Change (NM station)
5	23/02/1956	~ 5100% (Leeds)
42	29/29/1989	~ 340% (Calgary)
43	19/10/1989	~ 90% (South Pole)
44	22/10/1989	~ 190% (McMurdo)
45	24/10/1989	~ 200% (South Pole)
59	14/07/2000	~ 60% (South Pole)
60	15/04/2001	~ 220% (South Pole)

only contributes an increase of  $\sim 10\%$  in the ground-level muon flux. The exception in Figure 1.18 is for GLE 5, but this was an exceptionally large event, for which we haven't seen anything similar in over half a decade; such events are rare. We expect that we would have seen this increase in the HiSPARC data, but, of course, this event pre-dated the HiSPARC project.

These simulations, combined with the figures detailed in Table 1.2 and Table 1.3, show us that we would have expected an increase in the muon spectrum of no more than  $\sim 1\%$  (and more likely on the order of  $\sim 0.1\%$ ) for both GLE 71 and 72, which rules their observation with HiSPARC as extremely unlikely.

## 1.6 Standardisation of HiSPARC Data

### 1.6.1 Motivation

- HiSPARC stations are individually managed and guidelines aren't stringent
  - Variability between stations exists and also apparently between detectors within a station (i.e. see singles during GLE 72)
  - We have seen that the stations are sensitive to their local atmospheric conditions...

### 1.6.2 Barometric Correction

Observations made by ground-based CR detectors are susceptible to atmospheric conditions. Atmospheric pressure effects the CR path length due to the expansion

and contraction of the atmosphere with varying pressure; hence the CR counts are observed to be negatively correlated to atmospheric pressure as shown for both NMs and MDs in Figure 1.19. A correction for this barometric effect is routinely applied as part of the data calibration for all NM stations within the Neutron Monitor Data Base (NMDB) NEST, but there is no such process routinely applied in the HiSPARC networks data pipeline.

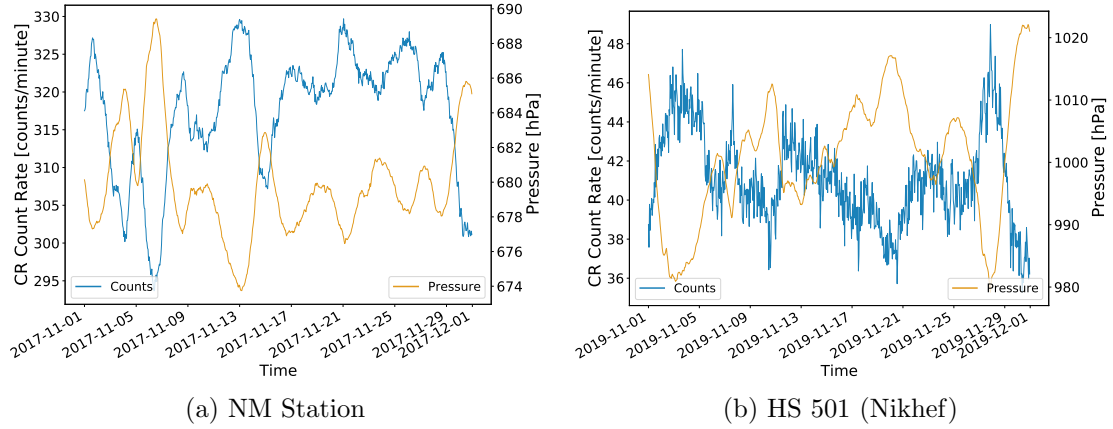


Figure 1.19: The anti-correlation between CR count rates and the atmospheric pressure. (a) shows the CR and the local atmospheric pressure measured at a NM in the South Pole; (b) shows the CR and pressure measured by HiSPARC station 501.

The method of correcting for the barometric effect is discussed widely in the literature regarding NMs and is shown to depend on the barometric coefficient. Assuming the cosmic ray flux variation, absent of the atmospheric effects, is reasonably stable, then a simple correction to the counts can be made. The CR variations ( $N$ ) that depend on the local atmospheric pressure are described by equation (1.2), where  $\Delta N$  is the change in count rate,  $\beta$  is the barometric coefficient, and  $\Delta P = P - P_0$  is the deviation in pressure from the average ( $P_0$ ) in the given time-period (Paschalidis et al., 2013):

$$\Delta N = -\beta N \Delta P \quad (1.2)$$

Through the integration of equation (1.2), the solution shows the dependence of cosmic ray intensity on pressure as given in equation (1.3).

$$N = N_0 e^{-\beta \Delta P} \quad (1.3)$$

Therefore by taking the logarithm of equation (1.3), one can obtain the barometric coefficient by fitting the straight line given by equation (1.4) to the observed data, where  $N_0$  may be assumed as the mean count rate over the given time-period of observations considered.

$$\ln \left( \frac{N}{N_0} \right) = -\beta \Delta P \quad (1.4)$$

A demonstration of the barometric correction method of fitting a straight line to the data described by equation (1.4) is shown for both a NM and a HiSPARC station in Figure 1.20.

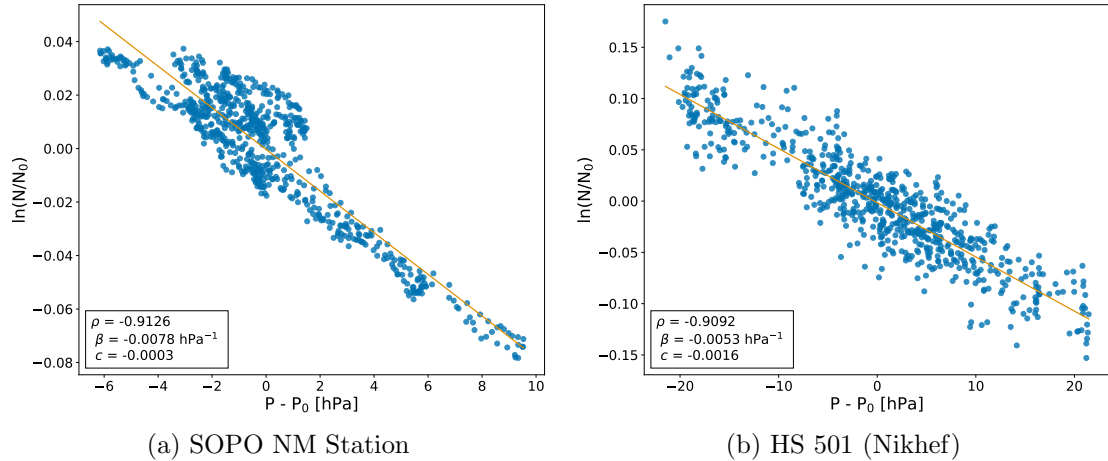


Figure 1.20: The barometric coefficient calculation: (a) during November 2017 for the South Pole (SOPO) NM station, (b) during November 2019 for HiSPARC station 501 at Nikhef.

An online barometric coefficient tool<sup>1</sup> is available for NMs, which allows users to perform the barometric correction for a given station over a user-defined epoch (Paschalis et al., 2013). Using this tool, it was possible to provide a comparison between the method used in this work to that of the online NM barometric correction tool which is used for the correction of the NMDB stations. This is provided in

---

<sup>1</sup><http://cosray.phys.uoa.gr/index.php/data/nm-barometric-coefficient>

Figure 1.21 for monthly corrections throughout 2017 for the NM station at the South Pole (SOPO).

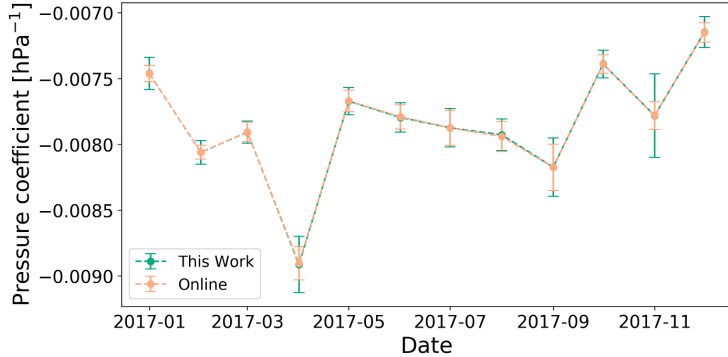


Figure 1.21: A comparison between the monthly barometric coefficient computed in this work and using the online barometric coefficient tool throughout the year 2017 for the SOPO NM station.

Figure 1.21 shows a close agreement between the barometric coefficient calculated in this work and those acquired from the online tool for the SOPO NM. This was also true for other stations tested (APTY and ROME), thus providing confidence that the method used in this work was suitable for application on the HiSPARC data. The barometric correction was performed on the stations where sufficient pressure data and count rates exist, and were re-investigated to determine whether the space weather events were observed in the HiSPARC data. These results are provided in Section 1.7.

[include a time series for the variation in the barometric coefficient for HiSPARC (i.e. for station 501)...]

### 1.6.3 Temperature Correction

It has been discussed in the literature that the effect of atmospheric temperature on muon intensity has to be treated differently to the pressure effect (Berkova et al., 2011), as the temperature influences both the creation and disintegration processes for muons, such that there is a positive effect and a negative effect on muon intensity as a consequence of temperature variations (Mendonça et al., 2016).

The positive effect is related to pion decay and its dependence on temperature

variation. The higher the temperature, the lower the atmospheric pion absorption, which implies a higher generation rate of muons (Mendon{\c{c}}a et al., 2016).

The negative effect corresponds to the decrease of muon intensity at ground level as the muon average path length varies with temperature. Due to the heating and the expansion of the atmosphere during summer periods muons are produced higher in the atmosphere; hence the muon propagation path increases meaning more atmosphere for muons to traverse before reaching the ground, and an increased decay probability and ionisation losses (Savi et al., 2015; Mendon{\c{c}}a et al., 2016).

Due to the difference in decay probability, the negative effects dominate for low energy muons (i.e. those detected by ground-level MDs), and the positive effect dominates for high energy muons (i.e. those detected by underground MDs) (Berkova et al., 2011); therefore it is expected that the negative effect should dominate for the HiSPARC network. Temperature effects are also observed by NMs; however the effect is less significant than for MDs hence temperature corrections are not widely applied for NMs (Mendon{\c{c}}a et al., 2016).

This is in contradiction with the observations of diurnal variation with the HiSPARC detector, as one can quite clearly see that the HiSPARC stations register higher count rates during local noon.

Several methods of correcting for the negative temperature effect are summarised by Berkova et al. (2011) which utilise different measures of atmospheric temperature when performing the temperature correction. Mendon{\c{c}}a et al. (2016) provides a comparative summary of these methods applied to correct for atmospheric temperature variations observed by GMDN detectors. The methods discussed here however are typically applied over long timescales of years with low temporal resolution rather than to account for short timescale variations with periods of less than a day; hence these methods aren't necessarily suitable for this work.

[finally discuss, in connection with the diurnal effect, that the HiSPARC stations don't really have a suitable measure of temperature. They provide the local outdoor

temperature, nearby, and also the temperature in the room where the electronics are (useless...)... so limited capacity to be able to do a good job on the temperature correction...]

## 1.7 HiSPARC Observations After Pressure Corrections

### 1.7.1 Pressure Corrected Observations of Ground Level Enhancements

Following the pressure correction, the search for evidence of GLEs was re-conducted, this time within the pressure corrected HiSPARC data. This could only be conducted for GLE 71 and 72, as the HiSPARC network was not collecting meteorological data during the epoch of GLE 70. Figure 1.22 and Figure 1.23 shows the pressure-corrected HiSPARC observations around the epochs of GLE 71 and 72, respectively.

The observations of GLE 71 show only the HiSPARC events data; however, we also show the singles rates from each of the individual detectors in a station for GLE 72.

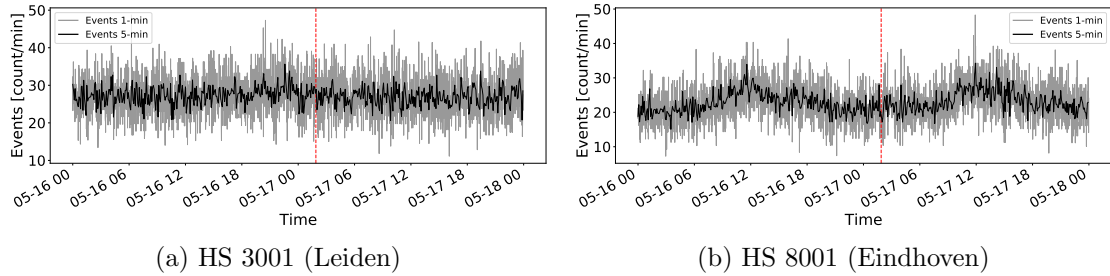


Figure 1.22: Pressure corrected HiSPARC data for 2 stations around the epoch of GLE 71. The top panel of each subplot shows the minute-averaged trigger events between detectors within the station, while the bottom panel shows the mean-shifted, minute-averaged counts by each individual detector in the station. The vertical red, dashed line depicts the approximate onset time of the GLE.

There are no clear GLEs observations in the pressure corrected HiSPARC data.

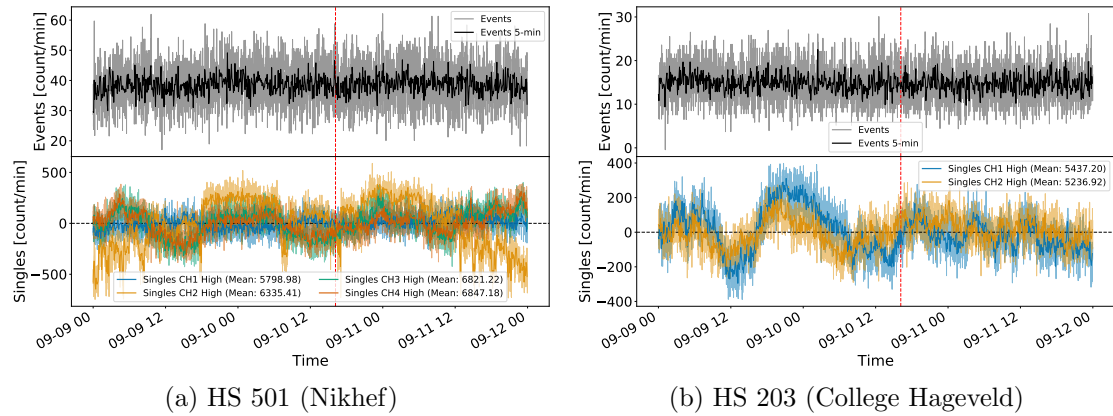


Figure 1.23: Pressure corrected HiSPARC data for 2 stations around the epoch of GLE 72. The top panel of each subplot shows the minute-averaged trigger events between detectors within the station, while the bottom panel shows the mean-shifted, minute-averaged counts by each individual detector in the station. The vertical red, dashed line depicts the approximate onset time of the GLE.

We believe this is due to the a mixture of the reasons discussed above: a high rigidity cut-off of the HiSPARC stations as GLEs are caused by SEPs with a lower energy, and too few additional muons produced during these most recent GLEs.

## 1.7.2 Pressure Corrected Observations of Forbush Decreases

The search for evidence of FDs was re-conducted, this time within the pressure corrected HiSPARC data. Figure 1.24 and Figure 1.25 shows the pressure-corrected HiSPARC observations around the epochs of a FD in July 2012 and December 2014, respectively.

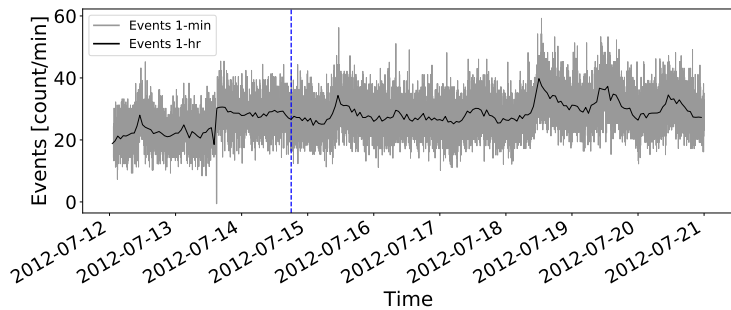


Figure 1.24: HS 8001 (Eindhoven)

There are no clear FDs observations in the pressure corrected HiSPARC data shown in Figure 1.24 and Figure 1.25...

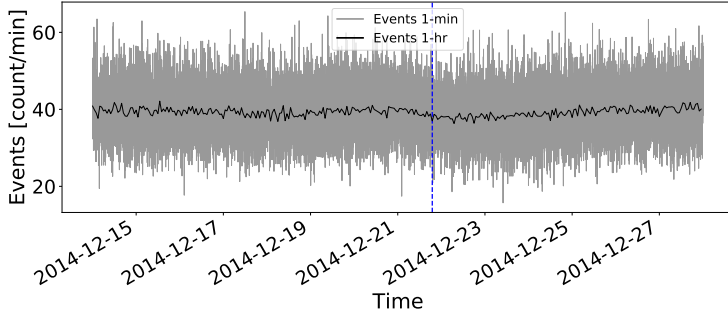


Figure 1.25: HS 501 (Nikhef)

[... introduce the last pressure corrected data plots...]

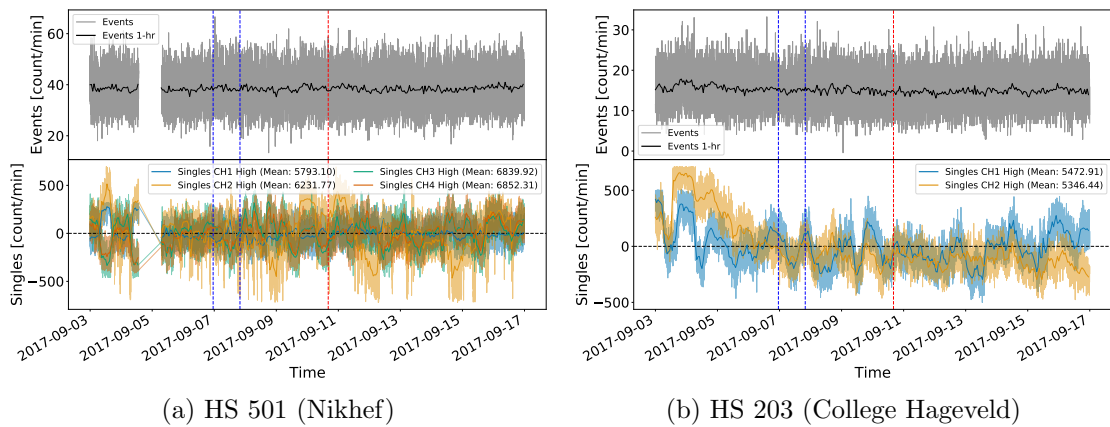


Figure 1.26: Pressure corrected HiSPARC data for 2 stations in an epoch where there were two FDs close to the onset of GLE 72. The top panel of each subplot shows the minute-averaged events data, while the bottom panels show the mean-shifted, minute-averaged counts by each individual detector in the stations. The vertical blue-dashed lines show the approximate onset-times of the FDs and the red-dashed line depicts the approximate onset-time of the GLE.

[...insert comments on the lack of clear fds here...]

## 1.8 Discussion

Throughout this chapter the feasibility of using the HiSPARC network of muon detectors has been analysed. This has involved performing cosmic ray air shower simulations using CORSIKA and performing backwards

## 1.9 Conclusion

...

We leave the reader with the following points:

1. ...

2. ...

3. ...

## 2 HiSPARC Station 14008

### 2.1 Introduction

It was clear from the work covered in Chapter 1, using data from the HiSPARC network, that the HiSPARC detectors were not clearly capable of observing space weather events and this is also hindered as they are rather sensitive to variations in the terrestrial conditions.

To some extent, it was possible to eliminate the variation in CRs due to terrestrial variation from the HiSPARC data; however it was shown to be not always so simple, as different detectors in the HiSPARC network showed different responses to pressure and temperature variation. The non-linear relationship between temperature and CR count means the correction of the count rate due to thermal fluctuations is non-trivial, unlike the counterpart correction for pressure.

It is believed that the atmospheric thermal fluctuations induce thermal noise in the Photo Multiplier Tubes (PMTs), and although the temperature inside the HiSPARC ski-boxes have not been measured, it is suspected that the PMTs can get quite hot, in particular when the sky boxes are in direct sunlight.

An instance of thermal noise in a single PMT will be random, and uncorrelated with an instance of thermal noise in another PMT. It is therefore possible to hypothesise that it is unlikely that within the coincidence window of  $\sim 1.5 \mu\text{s}$ , that a coincidence between 2 PMTs would be due to random thermal noise induced in the PMTs.

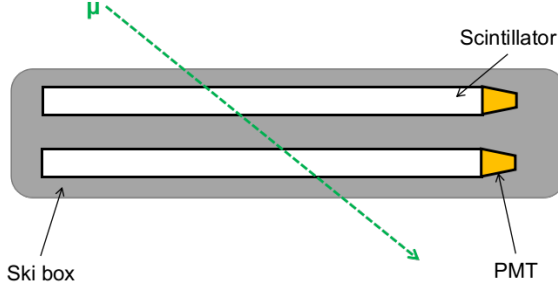


Figure 2.1: Schematic diagram of the HiSPARC station 14008 detector set-up.

To exploit this, it is possible to stack 2 detectors on top of each other to measure a single muon which traverses both scintillators, hence inducing signals in both PMTs.

## 2.2 Aims

The aim of creating a new HiSPARC station was to test whether an alternative configuration of HiSPARC station could minimise atmospheric deviations in the data and allow for the observation of space weather events...

## 2.3 HiSPARC 14008 Detector Set-up

### 2.3.1 Configuration

The configuration of HiSPARC station 14008 is shown in Figure 2.1; the station is composed of two scintillators stacked on top of each other, inside one ski-box.

Each of the plastic scintillators has a thickness of  $\Delta x = 0.5$  cm, and density,  $\rho = TBC \text{ gcm}^{-3}$ . We know that the stopping power of the scintillator for a minimum ionising particle is  $\sim 2 \text{ MeV/cm}^{-2}$  [REF]... [discuss this w/ Angela as it seems to be derivative of Blethe-Bloch, but cannot find link]...

$$E = \Delta x S \rho \cos(\theta) \quad (2.1)$$

Bartels (2012) state that typical energy loss of a muon in a single scintillator is 3.38 MeV, hence in this configuration, as a muon traverses two scintillators, the

lower limit on the energy loss by muons in the detector is  $\sim 6.76$  MeV.

To protect the scintillators and PMTs within the ski boxes, we sandwiched the scintillators between layers of foam, as can be seen on the lab work bench in Figure 2.2a. Upon complete assembly of the detector, the scintillators and PMTs are placed within the ski-box on the roof of the Poynting Physics building on the campus of the University of Birmingham, as shown in Figure 2.2b.

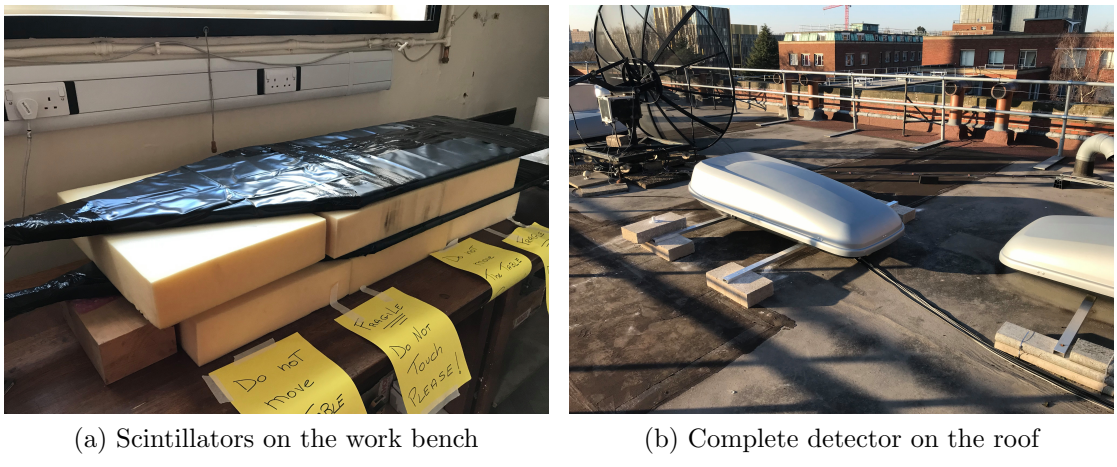


Figure 2.2: HiSPARC 14008 assembly and configuration. (a) shows the stacked arrangement of the scintillators on the lab work bench, between layers of protective foam. (b) shows the complete detector inside the ski-box on the University of Birmingham campus.

### 2.3.2 Calibration

When setting up the HiSPARC station, it was required to set several operating parameters for the detectors and the HiSPARC electronics box. One such setting was the PMT operating voltage. Each of the detector PMTs needs to be powered with a high enough operating voltage such to provide an amplified signal, but not too high such as to over-amplify the noise.

In general, the PMTs has an advised operating voltage of around 700 V (?); however, best practise is to operate the PMT at the plateau region, whereby the counts/voltage no longer increases. As can be seen from Figure 2.3, neither of the PMTs have clear plateau regions, hence there was no obvious PMT set point.

The HiSPARC installation manual does, however, suggest to tune the PMT

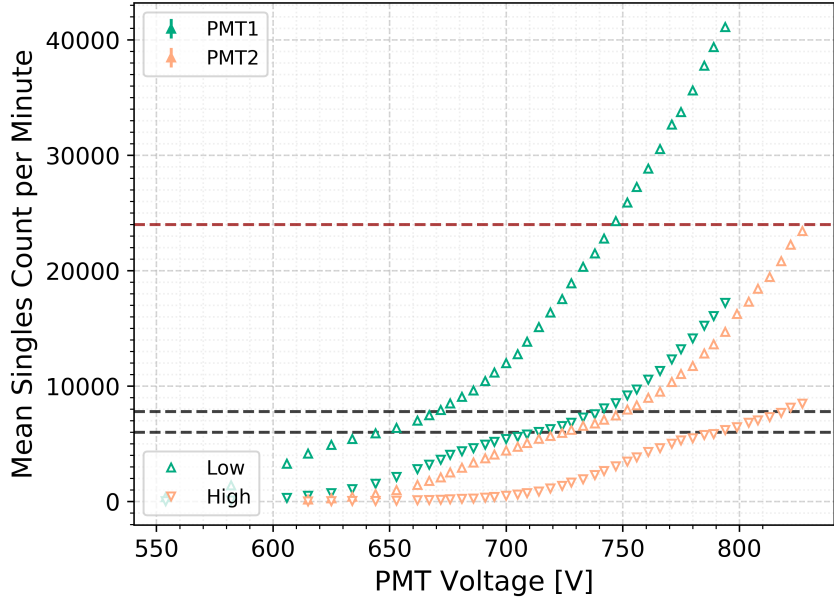


Figure 2.3: Voltage calibration curve for the PMTs of station 14008. The upper, red-dashed line indicates the upper limit for the low threshold singles rate (400 Hz), and the lower 2, black-dashed lines indicate the upper and lower bounds for the high threshold singles rate (100–130 Hz).

voltages such that the singles rates for each detector meet the following criteria: singles rate of 100–130 Hz for signal above the high trigger threshold, and singles rate of <400 Hz for signal above the low trigger threshold (?).

In order to calibrate the PMTs to the correct level, we measured the singles rates above the high and low thresholds as a function of PMT operating voltage, as is shown in Figure 2.3 [UPDATE THIS PLOT...!!!!]. The voltage calibration plot shows drastically the different performances one can get from different PMTs, therefore it is necessary to treat each PMT individually when calibrating.

### 2.3.3 Monitoring Temperature

It was suspected in Chapter 1 that the singles count rates (and thus event count rates also) are affected by the temperature of the PMT within the HiSPARC ski-boxes.

Some of the existing HiSPARC stations monitor local temperature however none measure the temperature of the PMT within the ski box; therefore the temperature of the PMT itself is unknown, and thus we cannot account for the thermal noise.

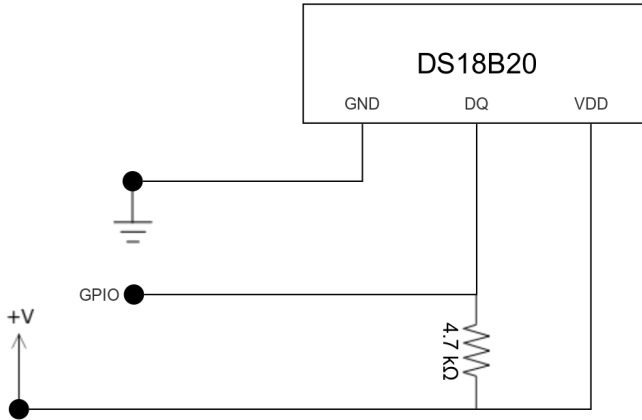


Figure 2.4: Schematic diagram of the DS18B20 temperature sensor circuit, whereby the voltage, ground, and GPIO interfaces connect directly into pins of the Raspberry Pi board.

When building this new HiSPARC station, a temperature sensor was placed into the ski box which allowed us to monitor the temperature.

Figure 2.4 shows the schematic for the temperature sensor. We used the DS18B20 temperature sensor with the one-wire telemetry protocol, which used a single wire to transmit the temperature readings to the microcontroller; the microcontroller used was a Raspberry Pi 4. Three wires were used for the operation of the DS18B20: constant current voltage, ground, and data.

We use the Raspberry Pi to control the data acquisition by running a Python program to output the temperature readings from the sensor to a local file. The temperature is read on a 10-second cadence and is recorded in degrees Celsius.

## 2.4 Observations

From the Cosmic Ray Simulations for Kascade (CORSIKA) simulations in the earlier section, we predict a ground level muon rate passing through the detectors...

(do this by integrating under curve, using 70-degree half-angle cone for solid angle, and area of  $0.5\text{m}^2$ )

Get the rate as:  $85.365 \mu/\text{s}$  (non-vertical, i.e. 70-deg sims) or  $156.924 \mu/\text{s}$  (for vertical sims)

... for a typical day with this station, we have a count rate of  $\sim 80 \mu/\text{s}$ ...

## **2.5 Conclusions**

# A Simulations of Cosmic Ray Air Showers using CORSIKA

There are several user-definable settings within Cosmic Ray Simulations for Cascade (CORSIKA). These settings are explained in-depth in the CORSIKA user's guide (Heck & Pierog, 2017). Here, the options selected when building and using CORSIKA are outlined.

For high energy, inelastic hadronic interactions within CORSIKA the QGSJET-II (Ostapchenko, 2006) model was selected. Interactions of hadrons with energies below 80 GeV are simulated using GHEISHA (Fesefeldt, 1985), which allowed for the simulation of PCRs in the regime of SCRs. In addition to these hadronic interactions, electromagnetic interactions within the CORSIKA simulations were described by the EGS4 (Nelson et al., 1985) model. Furthermore CORSIKA has a minimum muon energy limit that can be simulated of 10 MeV. This limit is sufficient, as the lowest energy muons that are observable with HiSPARC are those with energy of  $\sim 4$  MeV.

Simulation thinning was enable to reduce the computation time of the simulations and reduce the output file size. The observation level at which point the simulation cease was set at 100 m above sea level (compared to the  $\sim 50$  m typical of the stations; however, this difference is negligible for the air shower development). The pre-defined central European atmosphere in October was used for all simulations, and western-European magnetic field was used as calculated with the *Geomag*

programme [REF]:  $B_x = 18.799 \mu\text{T}$  and  $B_z = 44.980 \mu\text{T}$ .

Proton and  $\alpha$ -particle initiated air showers were generated with energies ranging from  $10^9$  to  $10^{20}$  eV, and  $4 \times 10^9$  to  $10^{20}$  eV, respectively. In total  $\sim 230000$  proton-initiated showers were simulated and  $\sim 180000$   $\alpha$ -particle-initiated air showers were simulated. The simulated air-shower-initiating PCRs are listed Table A.1 (proton) and Table A.2 ( $\alpha$ -particles).

Table A.1: Details of the proton-initiated air showers simulated using CORSIKA.

<b>E<sub>PCR</sub> (eV)</b>	<b>N<sub>sims</sub></b>	<b>E<sub>PCR</sub> (eV)</b>	<b>N<sub>sims</sub></b>
1.00E+09	10000	2.98E+12	1000
1.27E+09	10000	3.79E+12	1000
1.62E+09	10000	4.83E+12	1000
2.07E+09	10000	6.16E+12	1000
2.64E+09	10000	7.85E+12	1000
3.36E+09	10000	1.00E+13	1000
4.28E+09	10000	1.78E+13	100
5.46E+09	10000	3.16E+13	100
6.95E+09	10000	5.62E+13	100
8.86E+09	10000	1.00E+14	100
1.00E+10	10000	1.78E+14	50
1.13E+10	10000	3.16E+14	50
1.44E+10	10000	5.62E+14	50
1.83E+10	10000	1.00E+15	10
2.34E+10	10000	1.78E+15	10
2.98E+10	10000	3.16E+15	10
3.79E+10	10000	5.62E+15	10
4.83E+10	10000	1.00E+16	10
6.16E+10	10000	1.78E+16	10
7.85E+10	10000	3.16E+16	10
1.00E+11	10000	5.62E+16	10
1.27E+11	1000	1.00E+17	10
1.62E+11	1000	1.78E+17	10
2.07E+11	1000	3.16E+17	10
2.64E+11	1000	5.62E+17	10
3.36E+11	1000	1.00E+18	10
4.28E+11	1000	1.78E+18	10
5.46E+11	1000	3.16E+18	10
6.95E+11	1000	5.62E+18	10
8.86E+11	1000	1.00E+19	10
1.13E+12	1000	1.78E+19	10
1.44E+12	1000	3.16E+19	10
1.83E+12	1000	5.62E+19	10
2.34E+12	1000	1.00E+20	10

Table A.2: Details of the  $\alpha$ -particle-initiated air showers simulated using CORSIKA.

<b>E<sub>PCR</sub> (eV)</b>	<b>N<sub>sims</sub></b>	<b>E<sub>PCR</sub> (eV)</b>	<b>N<sub>sims</sub></b>
4.00E+09	10000	1.00E+13	1000
4.28E+09	10000	1.78E+13	100
5.46E+09	10000	3.16E+13	100
6.95E+09	10000	5.62E+13	100
8.86E+09	10000	1.00E+14	100
1.00E+10	10000	1.78E+14	50
1.13E+10	10000	3.16E+14	50
1.44E+10	10000	5.62E+14	50
1.83E+10	10000	1.00E+15	10
2.34E+10	10000	1.78E+15	10
2.98E+10	10000	3.16E+15	10
3.79E+10	10000	5.62E+15	10
4.83E+10	10000	1.00E+16	10
6.16E+10	10000	1.78E+16	10
7.85E+10	10000	3.16E+16	10
1.00E+11	10000	5.62E+16	10
1.27E+11	1000	1.00E+17	10
1.62E+11	1000	1.78E+17	10
2.07E+11	1000	3.16E+17	10
2.64E+11	1000	5.62E+17	10
3.36E+11	1000	1.00E+18	10
4.28E+11	1000	1.78E+18	10
5.46E+11	1000	3.16E+18	10
6.95E+11	1000	5.62E+18	10
8.86E+11	1000	1.00E+19	10
1.13E+12	1000	1.78E+19	10
1.44E+12	1000	3.16E+19	10
1.83E+12	1000	5.62E+19	10
2.34E+12	1000	1.00E+20	10
2.98E+12	1000		
3.79E+12	1000		
4.83E+12	1000		
6.16E+12	1000		
7.85E+12	1000		

# Bibliography

- Bartels R. T., 2012, Technical report, The HiSPARC Experiment: An Analysis of the MPV and the Number of Events per Unit Time. University College Utrecht
- Berkova M. D., Belov A. V., Eroshenko E. A., Yanke V. G., 2011, Bull. Russ. Acad. Sci. Phys., 75, 820
- Corti C., Potgieter M. S., Bindi V., Consolandi C., Light C., Palermo M., Popkow A., 2019, ApJ, 871, 253
- Desorgher L., Flckiger E. O., Gurtner M., 2006. p. 2361, <http://adsabs.harvard.edu/abs/2006cosp...36.2361D>
- ETEnterprises 2020, Technical Report 9125B, Data Sheet: 9125B Series, <http://et-enterprises.com/products/photomultipliers/product/p9125b-series>. ET Enterprises, <http://et-enterprises.com/products/photomultipliers/product/p9125b-series>
- Fesefeldt H., 1985, Technical Report PTHA-85/02, GHEISHA. The Simulation of Hadronic Showers: Physics and Applications. RWTH Aachen
- Fokkema D. B. R. A., 2012, PhD thesis, University of Twente
- Heck D., Pierog T., 2017, Technical Report 7.6400, Extensive Air Shower Simulation with CORSIKA: A Users Guide
- Herbst K., Kopp A., Heber B., 2013, Annales Geophysicae, 31, 1637
- Lingri D., Mavromichalaki H., Belov A., Eroshenko E., Yanke V., Abunin A., Abunina M., 2016, arXiv:1612.08900 [astro-ph]
- Mendon{\c{c}}a R. R. S. d., et al., 2016, ApJ, 830, 88
- NMDB 2018, NMDB Event Search Tool (NEST), <http://www.nmdb.eu/nest/>
- Nelson W. R., Hirayama H., Rogers D. W. O., 1985, Technical Report SLAC-265, EGS4 code system, <https://www.osti.gov/biblio/6137659-egs4-code-system>. Stanford Linear Accelerator Center, Menlo Park, CA (USA), <https://www.osti.gov/biblio/6137659-egs4-code-system>
- Ostapchenko S., 2006, Nuclear Physics B - Proceedings Supplements, 151, 143
- Paschalis P., Mavromichalaki H., Yanke V., Belov A., Eroshenko E., Gerontidou M., Koutroumpi I., 2013, New Astronomy, 19, 10

Savi M., Maleti D., Jokovi D., Veselinovi N., Banjanac R., Udovii V., Dragi A., 2015, J. Phys.: Conf. Ser., 632, 012059

van Dam K., van Eijk B., Fokkema D. B. R. A., van Holten J. W., de Laat A. P. L. S., Schultheiss N. G., Steijger J. J. M., Verkooijen J. C., 2020, Nuclear Instruments and Methods in Physics Research Section A: Accelerators, Spectrometers, Detectors and Associated Equipment, 959, 163577